High-Reynolds-number flow

10

Having discussed viscous flow at low Reynolds numbers in Chapter 9, now we turn our attention to the diametrically opposite limit of inertia-dominated flow at high Reynolds numbers. Inspecting the changes in the structure of a flow with increasing Reynolds number, we encounter a rich phenomenology and a variety of transition protocols. In all cases, when the Reynolds number exceeds a critical threshold, flow instability sets in and a small-scale turbulent motion is established. The study of the structure and dynamics of flow at high Reynolds numbers encompasses several complementary topics including potential flow theory, boundary-layer analysis, hydrodynamic stability, turbulent flow, and vortex motion. Potential flow was discussed earlier in this book; boundary-layer theory, hydrodynamic stability, and turbulent motion are discussed in this chapter; vortex motion is the exclusive topic of Chapter 11.

10.1 Changes in the structure of a flow with increasing Reynolds number

As the Reynolds number of a flow increases by raising, for example, the magnitude of the velocity, the structure of the flow changes in a way that depends strongly on the particular flow configuration. Even though a general statement regarding the anticipated protocol of change cannot be made, several pervasive features can be identified.

C. Pozrikidis, *Fluid Dynamics*, DOI 10.1007/978-1-4899-7991-9_10

Boundary layers

As the Reynolds number increases, diffusion of vorticity away from the boundaries of the flow and into the bulk of the fluid is hindered by strong convection along the boundaries, toward the boundaries, or both. As a result, vorticity tends to be confined inside boundary layers and within free shear layers developing along fluid interfaces and free surfaces. Viscous forces are significant inside the boundary and free shear layers, but can be neglected in the bulk of the flow.

Vortices

Vorticity that has entered the flow by diffusion across the boundaries may accumulate into compact regions of rotational motion identified as vortices. Vortices are typically generated behind bluff bodies and at the trailing edge of streamlined objects.

Vortex dynamics

Vortex interaction causes the flow to become unsteady in a deterministic, random, or chaotic fashion. Spatial, temporal, and spatio-temporal chaos can be established even at moderate Reynolds numbers.

Instability

When the Reynolds number exceeds a critical threshold, small disturbances amplify, altering the local and sometimes the global structure of a flow.

Transition to turbulence

Instability is followed by transition leading to turbulent flow where a small-scale unsteady motion is superimposed on a large-scale steady or unsteady flow. The small-scale motion affects and is affected significantly by the large-scale structure and global properties of the flow.

10.1.1 Flow past a cylinder

The salient changes in the structure of streaming (uniform) flow past a circular cylinder with increasing Reynolds number, $\mathrm{Re} \equiv \rho D U/\mu$, are illustrated in Figure 10.1.1(a). In the definition of the Reynolds number, D is the cylinder diameter, U is the velocity of the approaching stream far from the cylinder, μ is the fluid viscosity, and ρ is the fluid density.

When the Reynolds number is less than unity, inertial forces are negligible near the cylinder. The motion of the fluid is governed by the equations of Stokes flow discussed in Chapter 9, and the streamline pattern is symmetric with respect to the vertical plane that is normal to the incident stream and passes through the cylinder mid-plane.

As the Reynolds number increases, inertial forces become increasingly significant, and a boundary layer, identified as a region of increased vorticity, is established around the surface of the cylinder. The rotational fluid inside the boundary layer is convected along

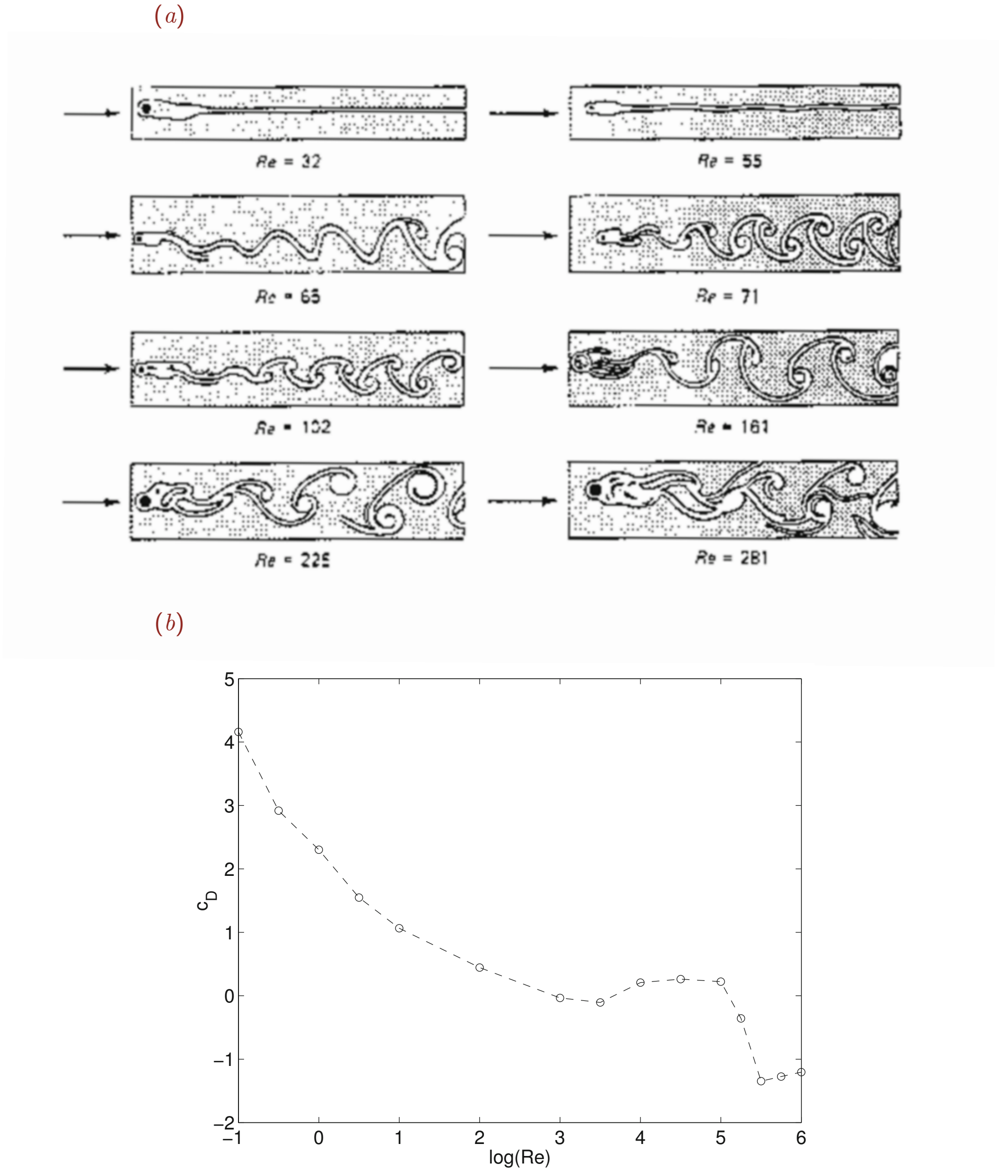

Figure 10.1.1 (*a*) Schematic illustration of changes in the structure of streaming flow past a circular cylinder with increasing Reynolds numbers, showing boundary-layer separation and the development of a wake, after *Homann, F.* (1936) Einfluss grosser zähigkeit bei strömung um zylinder. *Forschg. Ing.-Wes.* **7**, 1–10. (*b*) Drag coefficient plotted against the Reynolds number defined with respect to the cylinder diameter.

the cylinder and accumulates behind the cylinder to form two regions of recirculating flow, leading to a slender wake.

A further increase in the Reynolds number causes the flow to become unstable. A pair of vortices developing behind the cylinder are shed downstream in an alternating fashion at a frequency that depends weakly on the Reynolds number, only to be replenished by newly formed vortices. The frequency of shedding, f, is expressed by the dimensionless Strouhal number, $\mathrm{St} \equiv fD/U$. In the case of a circular cylinder, laboratory observations show that $\mathrm{St} \simeq 0.2$. Far from the cylinder, the wake consists of two rows of counter-rotating vortices arranged in a staggered configuration that is known as the von Kàrmàn vortex street. At even higher Reynolds numbers, turbulent flow is established and the edges of the wake become blurred and poorly defined.

Behavior of the drag force

The changes in the structure of the flow described previously in this section have a strong influence on the drag force exerted on the cylinder. A graph of the dimensionless drag coefficient,

$$c_{\mathrm{D}} \equiv \frac{2F}{\rho D U^2}, \tag{10.1.1}$$

is plotted against the Reynolds number in Figure 10.1.1(b) on a log-log scale, where F is the drag force per unit length exerted on the cylinder.

In the limit of vanishing Reynolds number, $\mathrm{Re} \to 0$, theoretical analysis shows that the drag force is given by the modified Stokes law

$$F \simeq \frac{4\pi}{\ln \frac{7.4}{\mathrm{Re}}} \, \mu U. \tag{10.1.2}$$

Correspondingly, the drag coefficient is given by

$$c_{\mathrm{D}} \simeq \frac{8\pi}{\mathrm{Re} \, \log \frac{7.4}{\mathrm{Re}}}. \tag{10.1.3}$$

The change in the functional form of the drag coefficient at a critical Reynolds number on the order of 10^3, evident in Figure 10.1.1(b), is due to the detachment of the boundary layer from the surface of the cylinder at a certain point at the rear surface of the cylinder, as discussed in Section 10.4. The detachment occurs in a process that is described as flow separation.

When the Reynolds number becomes on the order of 10^5, the flow becomes turbulent and the boundary layer reattaches, causing a sudden decline in the drag coefficient as shown in Figure 10.1.1(b).

The non-monotonic dependence of the force drag coefficient on the Reynolds number illustrated in Figure 10.1.1(b) is a manifestation of the complexity of fluid motion in high Reynolds number flow.

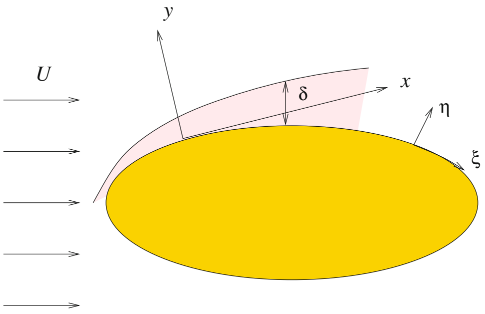

Figure 10.2.1 Schematic illustration of a Prandtl boundary layer developing around the surface of a two-dimensional curved body.

PROBLEM

10.1.1 *Flow in a channel through an expansion*

Consider flow through a channel with a sudden expansion, as illustrated in Figure 6.2.1. Discuss the expected changes in the structure of the flow with increasing a properly defined Reynolds number.

10.2 Prandtl boundary-layer analysis

In Section 10.1, we identified a boundary layer as a region of elevated vorticity over a solid boundary in a high-Reynolds-number flow. To make the concept of a boundary layer more specific, we may consider a model flow consisting of the following two regimes:

- An outer regime where the curl of the vorticity or the vorticity itself vanishes and the motion of the fluid is described by the equations of inviscid flow, including Euler's equation and the continuity equation.
- A boundary layer across which the vorticity undergoes a rapid transition and the magnitude of viscous forces is significant, as illustrated in Figure 10.2.1.

Wakes and regions of recirculating flow are allowed, but are significant only insofar as to determine the structure of the outer flow.

10.2.1 Simplifications

The slenderness of the boundary layer, compared with the typical size of the boundaries, flow allows us to simplify the equation of motion for the flow inside the boundary layer, and thereby derive approximate solutions in the asymptotic limit of high Reynolds numbers, $\mathrm{Re} \to \infty$.

To illustrate the physical arguments involved in the formulation of the boundary-layer theory, and simultaneously demonstrate the salient mathematical simplifications, we consider the boundary layer developing along a mildly-curved two-dimensional rigid body that is held stationary in an incident irrotational flow, as shown in Figure 10.2.1. Extensions to axisymmetric and three-dimensional flow are straightforward.

Continuity equation

We begin the analysis by introducing Cartesian coordinates where the x axis is tangential to the body at a point and the y axis is perpendicular to the body at that point, as shown in Figure 10.2.1. Next, we apply the continuity equation for two-dimensional flow at a point in the vicinity of the origin,

$$\frac{\partial u_x}{\partial x} + \frac{\partial u_y}{\partial y} = 0. \tag{10.2.1}$$

Let L be is the typical dimension of the body, U be the magnitude of the velocity of the incident irrotational flow, δ be the designated thickness of the boundary layer, and V be the typical magnitude of component of the velocity normal to the body at the edge of the boundary layer.

It is reasonable to expect that the magnitude of the derivative $\partial u_x/\partial x$ inside the boundary layer will be comparable to the ratio U/L, while the magnitude of the derivative $\partial u_y/\partial y$ will be comparable to the ratio V/δ. The continuity equation (10.2.1) requires that

$$\frac{U}{L} \sim \frac{V}{\delta} \qquad \text{or} \qquad V \sim \frac{U}{L}\,\delta, \tag{10.2.2}$$

which shows that the normal component of the velocity at the edge of the boundary layer scales with the boundary-layer thickness, δ.

x component of the equation of motion

Next, we examine the two components of the equation of motion in the vicinity of the origin written for the dynamic pressure that excludes hydrostatic variations, defined as

$$\varsigma \equiv p - \rho\,\mathbf{g}\cdot\mathbf{x}. \tag{10.2.3}$$

Considering the x component of the Navier–Stokes equation,

$$\frac{\partial u_x}{\partial t} + \underset{\displaystyle \frac{U^2}{L}}{\underset{\downarrow}{u_x \frac{\partial u_x}{\partial x}}} + \underset{\displaystyle \frac{U^2}{L}}{\underset{\downarrow}{u_y \frac{\partial u_x}{\partial y}}} = -\frac{1}{\rho}\frac{\partial \varsigma}{\partial x} + \nu\,(\underset{\displaystyle \nu\,\frac{U}{L^2}}{\underset{\downarrow}{\frac{\partial^2 u_x}{\partial x^2}}} + \underset{\displaystyle \nu\,\frac{U}{\delta^2}}{\underset{\downarrow}{\frac{\partial^2 u_x}{\partial y^2}}}), \tag{10.2.4}$$

we scale u_x with U, $\partial u_x/\partial x$ with U/L, u_y with V, $\partial u_x/\partial y$ with U/δ, the second derivative $\partial^2 u_x/\partial x^2$ with U/L^2, and the second derivative $\partial^2 u_x/\partial y^2$ with U/δ^2.

Moreover, we use the scaling shown in (10.2.2) to eliminate V in favor of U, and find that the magnitude of the various terms is as shown underneath equation (10.2.5). The scaling of the first term involving the time derivative on the left-hand side is determined by the temporal variation of the outer flow, which is best left unspecified. At this stage, there is no obvious way of scaling the x derivative of the dynamic pressure gradient on the right-hand side of (10.2.5) on the basis of kinematics alone.

The scalings shown underneath equation (10.2.5), combined with the assumption $\delta \ll L$, have two important consequences. First, the penultimate viscous term on the right-hand side is small compared to the last viscous term and may be neglected, yielding the boundary-layer equation

$$\frac{\partial u_x}{\partial t} + u_x \frac{\partial u_x}{\partial x} + u_y \frac{\partial u_x}{\partial y} = -\frac{\partial \varsigma}{\partial x} + \nu \frac{\partial^2 u_x}{\partial y^2}. \tag{10.2.5}$$

Second, the magnitude of the last viscous term must be comparable to the magnitude of the inertial terms on the left-hand side, so that

$$\frac{U^2}{L} \sim \nu \frac{U}{\delta^2} \tag{10.2.6}$$

or

$$\delta \sim \sqrt{\frac{\nu L}{U}} = \frac{L}{\sqrt{\mathrm{Re}}}, \tag{10.2.7}$$

where $\mathrm{Re} = UL/\nu$ is the Reynolds number defined with respect to the boundary size, L.

y component of the equation of motion

Next, we consider the individual terms in the y component of the equation of motion,

$$\frac{\partial u_y}{\partial t} + \underset{\substack{\downarrow \\ \frac{U^2\delta}{L^2}}}{u_x \frac{\partial u_y}{\partial x}} + \underset{\substack{\downarrow \\ \frac{U^2\delta}{L^2}}}{u_y \frac{\partial u_y}{\partial y}} = -\frac{1}{\rho}\frac{\partial \varsigma}{\partial y} + \nu \Big(\underset{\substack{\downarrow \\ \frac{U^2\delta}{L^2}}}{\frac{\partial^2 u_y}{\partial x^2}} + \underset{\substack{\downarrow \\ \frac{U^2\delta}{L^2}}}{\frac{\partial^2 u_y}{\partial y^2}} \Big), \tag{10.2.8}$$

and scale u_y with V, $\partial u_y/\partial x$ with V/L, u_x with U, $\partial u_y/\partial y$ with V/δ, the second derivative $\partial^2 u_y/\partial x^2$ with V/L^2, and the second derivative $\partial^2 u_y/\partial y^2$ with V/δ^2. Moreover, we express the kinematic viscosity of the fluid, ν, in terms of δ using the first equation in (10.2.7), replacing it with $U\delta^2/L$, and find that the magnitude of the various terms is as shown underneath equation (10.2.8).

The magnitude of all nonlinear convective and viscous terms is of order δ. Unless the magnitude of the temporal derivative on the left-hand side is of order unity, the dynamic pressure gradient across the boundary layer must also be of order δ, $\partial\varsigma/\partial y \sim \delta$,; to leading-order approximation,

$$\frac{\partial \varsigma}{\partial y} \simeq 0. \tag{10.2.9}$$

We conclude that non-hydrostatic pressure variations across the boundary layer are negligible and the dynamic pressure inside the boundary layer is primarily a function of position along the boundary measured by the arc length.

10.2.2 Boundary-layer equations

To compute the streamwise pressure gradient, we evaluate the x component of the Euler equation (6.4.3) at the edge of the boundary layer, obtaining

$$-\frac{1}{\rho}\frac{\partial\varsigma}{\partial x} = \frac{\partial U_x}{\partial t} + U_x\,\frac{\partial U_x}{\partial x}, \tag{10.2.10}$$

where U_x is the tangential component of the velocity of the outer flow. The boundary-layer equation (10.2.5) then becomes

$$\frac{\partial u_x}{\partial t} + u_x\,\frac{\partial u_x}{\partial x} + u_y\,\frac{\partial u_x}{\partial y} = \frac{\partial U_x}{\partial t} + U_x\,\frac{\mathrm{d}U_x}{\mathrm{d}x} + \nu\,\frac{\partial^2 u_x}{\partial y^2} \tag{10.2.11}$$

in a general unsteady flow.

Equations (10.2.1) and (10.2.11) provide us with a system of two second-order, nonlinear partial-differential equations for the velocity components u_x and u_y. The solution is subject to two sets of conditions: (a) the no-slip and no-penetration boundary conditions requiring that u_x and u_y are zero along the boundary, and (b) a far-field condition requiring that, as y/δ tends to infinity, u_x tends to the tangential component of the outer velocity, U_x. Because the boundary-layer equations do not involve the second partial derivative of u_y with respect to y, a far-field condition for u_y is not required.

In the boundary-layer analysis, the pressure is computed by solving the equations governing the structure of the outer irrotational flow.

Favorable and adverse pressure gradient

Evaluating equation (10.2.11) at the origin of the local Cartesian coordinates, and enforcing the no-slip and no-penetration boundary conditions in a steady flow, we obtain

$$\left(\frac{\partial^2 u_x}{\partial y^2}\right)_{y=0} = -\frac{1}{\nu}\,U_x\,\frac{\mathrm{d}U_x}{\mathrm{d}x}, \tag{10.2.12}$$

which shows that the sign of the curvature of the velocity profile at the boundary is opposite to that of the streamwise acceleration of the outer flow, $\mathrm{d}U_x/\mathrm{d}x$. Thus, the flow inside the boundary layer in a decelerating outer flow ($\mathrm{d}U/\mathrm{d}x < 0$) reverses direction, causing convection of vorticity away from the boundary and the consequent formation of vortices in the bulk of the flow.

When $\mathrm{d}U_x/\mathrm{d}x > 0$, the pressure gradient is negative, $\mathrm{d}\varsigma/\mathrm{d}x < 0$, and the boundary layer is subjected to a favorable pressure gradient. In the opposite case where $\mathrm{d}U_x/\mathrm{d}x < 0$, the pressure gradient is positive, $\mathrm{d}\varsigma/\mathrm{d}x > 0$, and the boundary layer is subjected to an adverse pressure gradient. Equation (10.2.12) shows that an adverse pressure gradient promotes flow separation.

10.2.3 Surface curvilinear coordinates

The Prandtl boundary-layer equation (10.2.11) was developed with reference to the local Cartesian axes shown in Figure 10.2.1, and is strictly valid near the origin of the local Cartesian coordinates. To avoid redefining the Cartesian axes at every point along a boundary, we introduce curvilinear coordinates where the ξ axis is tangential to the boundary and the η axis is perpendicular to the boundary, as shown in Figure 10.2.1. The corresponding velocity components are denoted by u_ξ and u_η.

Repeating the boundary-layer analysis, we find that the boundary-layer equations stated in (10.2.1), (10.2.9), and (10.2.11) stand true to leading-order approximation, provided that the Cartesian x and y coordinates are replaced by corresponding arc lengths in the ξ and η directions denoted, respectively, by ℓ_ξ and ℓ_η. Equation (10.2.9) becomes

$$\frac{\partial \varsigma}{\partial \ell_\eta} = \kappa \, \rho \, U_\xi^2, \tag{10.2.13}$$

where κ is the curvature of the boundary. Thus, the dynamic pressure drop across the boundary layer is of order δ, provided that κ is not too large; that is, provided that the boundary is not too sharply curved.

For simplicity, in the remainder of this chapter we denote ℓ_ξ and ℓ_η, respectively, by x and y.

10.2.4 Parabolization

The absence of a second partial derivative with respect to the streamwise position, x, renders the boundary-layer equation (10.2.11) a parabolic partial differential equation in x. This classification has important consequences on the nature of the solution and chosen numerical method of computing the solution.

Most important, the system of equations (10.2.1) and (10.2.11) can be solved using a marching method with respect to x, beginning from a particular x station where the structure of the boundary layer is somehow known; examples will be discussed later in this chapter. In contrast, because the Navier–Stokes equation is an elliptic partial differential equation with respect to x and y, the solution must by found simultaneously at every point in the flow, even when the velocity and pressure at the inlet are specified.

The parabolic nature of (10.2.11) with respect to x implies that, if a perturbation is introduced at some point along the boundary layer, it will modify the structure of the flow downstream but will leave the upstream flow unaffected. The absence of the second partial derivative with respect to x due to the boundary-layer approximation precludes a mechanism for upstream signal propagation.

10.2.5 Flow separation

Boundary-layer analysis for laminar flow is based on two key assumptions: (a) the Reynolds number is sufficiently large, but not so large that the flow becomes turbulent, and (b) and

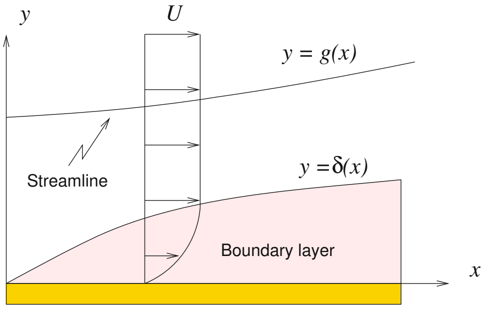

Figure 10.3.1 Schematic illustration of the boundary layer developing along a semi-infinite flat plate that is held parallel to a uniform incident stream.

the vorticity remains confined inside boundary layers wrapping around the boundaries. The physical relevance of the second assumption depends on the structure of the incident flow and on the geometry of the boundaries.

Streamlined bodies allow laminar boundary layers to develop over a large portion of their surface, whereas bluff bodies cause the vorticity to concentrate inside compact regions forming steady or unsteady wakes. For example, the alternating ejection of vortices of opposite sign into a wake is responsible for the von Kàrmàn vortex street illustrated in Figure 10.1.1(a). These limitations should be born in mind when questioning the physical relevance of results based on the boundary-layer approximation.

PROBLEM

10.2.1 *Oscillatory flow over a plate*

Compute the velocity profile in the boundary layer along an infinite plate driven by a streaming oscillatory outer flow with velocity $U_x = \overline{U}_x \cos(\omega t)$, where $\overline{U}_x$ is is the amplitude and ω is the angular frequency of the oscillations.

10.3 Blasius boundary layer on a semi-infinite plate

Having established a simplified equation of motion for the flow inside a boundary layer over a solid surface, we proceed to derive solutions by analytical and numerical methods. In this section, we study the boundary layer established over a semi-infinite flat plate that is held stationary parallel to an incident streaming (uniform) flow with velocity U, as illustrated in Figure 10.3.1.

Since the tangential velocity of the outer flow is constant, $\mathrm{d}U_x/\mathrm{d}x = 0$, the boundary-layer equation (10.2.11) for steady flow simplifies to a convection–diffusion equation for the streamwise velocity component,

$$u_x \frac{\partial u_x}{\partial x} + u_y \frac{\partial u_x}{\partial y} = \nu \frac{\partial^2 u_x}{\partial y^2}. \tag{10.3.1}$$

The problem has been reduced to solving the simplified equation of motion (10.3.1), together with the continuity equation (10.2.1), for the velocity components, u_x and u_y, subject to the no-slip, no-penetration, and far-field conditions.

Scaling

Because the length of the plate is infinite, the only available characteristic length scale, L, introduced in Section 10.2, is the streamwise distance from the leading edge, x. The second relation in (10.2.7) then provides us with an expression for the boundary-layer thickness in terms of the local Reynolds number, $\mathrm{Re}_x \equiv Ux/\nu$,

$$\delta(x) \sim \sqrt{\frac{\nu x}{U}} = \frac{x}{\sqrt{\mathrm{Re}_x}}. \tag{10.3.2}$$

Recall that this scaling has arisen by balancing the magnitude of inertial and viscous forces inside the boundary layer.

10.3.1 Self-similarity and the Blasius equation

Blasius discovered that computing the solution of the system of partial differential equations (10.2.1) and (10.3.1) can be reduced solving a single ordinary differential equation. To carry out this reduction, we assume that the flow develops in a self-similar fashion, such that the streamwise velocity profile across the boundary layer is a function of a scaled dimensionless transverse position expressed by the similarity variable

$$\eta \equiv \frac{y}{\delta(x)} = y \sqrt{\frac{U}{\nu x}} \tag{10.3.3}$$

according to the functional form

$$u_x(x, y) = U\, F(\eta), \tag{10.3.4}$$

where $F(\eta)$ is an *a priori* unknown function.

A key observation is that this self-similar streamwise profile derives from the stream function

$$\psi(x, y) = \sqrt{\nu\, U x}\, f(\eta), \tag{10.3.5}$$

where f is the indefinite integral or anti-derivative of F, satisfying $\mathrm{d}f/\mathrm{d}\eta = F$. The principal advantage of using the stream function is that the continuity equation is satisfied automatically and does not need to be considered.

As a preliminary, we compute the derivatives

$$\frac{\partial \eta}{\partial x} = -\frac{y}{2x}\sqrt{\frac{U}{\nu x}}, \qquad \frac{\partial \eta}{\partial y} = \sqrt{\frac{U}{\nu x}}. \tag{10.3.6}$$

Differentiating (10.3.5) with respect to y or x and setting

$$\frac{\partial f}{\partial x} = \frac{\mathrm{d}f}{\mathrm{d}\eta}\frac{\partial \eta}{\partial x}, \qquad \frac{\partial f}{\partial y} = \frac{\mathrm{d}f}{\mathrm{d}\eta}\frac{\partial \eta}{\partial y}, \tag{10.3.7}$$

we derive the x velocity component,

$$u_x(x,y) = \frac{\partial \psi}{\partial y} = U\sqrt{\nu\, U x}\,\frac{\mathrm{d}f}{\mathrm{d}\eta}\,\frac{\mathrm{d}\eta}{\mathrm{d}y} = U\sqrt{\nu\, U x}\,\frac{\mathrm{d}f}{\mathrm{d}\eta}\sqrt{\frac{U}{\nu x}}, \tag{10.3.8}$$

yielding

$$\boxed{u_x(x,y) = U\,\frac{\mathrm{d}f}{\mathrm{d}\eta},} \tag{10.3.9}$$

and the y velocity component

$$u_y(x,y) = -\frac{\partial \psi}{\partial x} = -(U\nu)^{1/2}\,\frac{\partial[\sqrt{x}\,f(\eta)]}{\partial x}, \tag{10.3.10}$$

yielding

$$u_y(x,y) = -\tfrac{1}{2}\sqrt{\frac{U\nu}{x}}\,f - \sqrt{\nu U x}\,\frac{\mathrm{d}f}{\mathrm{d}\eta}\,\frac{\partial \eta}{\partial x} \tag{10.3.11}$$

and then

$$\boxed{u_y(x,y) = -\tfrac{1}{2}\sqrt{\frac{U\nu}{x}}\,\Big(f - \eta\,\frac{\mathrm{d}f}{\mathrm{d}\eta}\Big).} \tag{10.3.12}$$

Further differentiation yields

$$\frac{\partial u_x}{\partial x} = U\,\frac{\mathrm{d}^2 f}{\mathrm{d}\eta^2}\,\frac{\partial \eta}{\partial x}, \qquad \frac{\partial u_x}{\partial y} = U\,\frac{\mathrm{d}^2 f}{\mathrm{d}\eta^2}\,\frac{\partial \eta}{\partial y}, \tag{10.3.13}$$

and

$$\frac{\partial^2 u_x}{\partial y^2} = U\,\frac{\mathrm{d}^3 f}{\mathrm{d}\eta^3}\Big(\frac{\partial \eta}{\partial y}\Big)^2. \tag{10.3.14}$$

Substituting these expressions into the boundary-layer equation (10.3.1) and simplifying, we obtain a third-order nonlinear ordinary differential equation for the function $f(\eta)$,

$$\boxed{\frac{\mathrm{d}^3 f}{\mathrm{d}\eta^3} + \tfrac{1}{2}\,f\,\frac{\mathrm{d}^2 f}{\mathrm{d}\eta^2} = 0,} \tag{10.3.15}$$

derived by Blasius in 1908.

Enforcing the no-slip and no-penetration conditions and requiring that the flow in the boundary layer reduces to the outer uniform flow far from the plate, we obtain

$$f = 0 \quad \text{and} \quad \frac{\mathrm{d}f}{\mathrm{d}\eta} = 0 \quad \text{at} \quad \eta = 0, \tag{10.3.16}$$

and

$$\frac{\mathrm{d}f}{\mathrm{d}\eta} \to 1 \quad \text{as} \quad \eta \to \infty. \tag{10.3.17}$$

These equations provide us with boundary and far-field conditions to be used in solving the Blasius equation (10.3.15).

Before proceeding to compute the solution, it is instructive to apply the Blasius equation (10.3.15) at the plate where $\eta = 0$. Using the first boundary condition in (10.3.16), we find that

$$\left(\frac{\mathrm{d}^3 f}{\mathrm{d}\eta^3}\right)_{\eta=0} = 0, \tag{10.3.18}$$

which shows that the curvature of the streamwise velocity profile vanishes at the wall, in agreement with equation (10.2.12).

10.3.2 Numerical solution

To solve the Blasius equation (10.3.15), it is convenient to rename $x_1 = f$, denote the first and second derivative of the function f as

$$x_2 \equiv \frac{\mathrm{d}f}{\mathrm{d}\eta}, \qquad x_3 \equiv \frac{\mathrm{d}x_2}{\mathrm{d}\eta} = \frac{\mathrm{d}^2 f}{\mathrm{d}\eta^2}, \tag{10.3.19}$$

and resolve the third-order equation into a system of three first-order nonlinear equations,

$$\frac{\mathrm{d}x_1}{\mathrm{d}\eta} = x_2, \qquad \frac{\mathrm{d}x_2}{\mathrm{d}\eta} = x_3, \qquad \frac{\mathrm{d}x_3}{\mathrm{d}\eta} = -\tfrac{1}{2}\, x_1\, x_3. \tag{10.3.20}$$

This system is accompanied by three boundary conditions,

$$x_1(\eta = 0) = 0, \qquad x_2(\eta = 0) = 0, \qquad x_3(\eta = \infty) = 1, \tag{10.3.21}$$

originating from (10.3.16) and (10.3.17).

Shooting method

Since boundary conditions are provided at both ends of the solution domain with respect to η, extending from 0 to ∞, we are presented with a two-point boundary-value problem involving three first-order differential equations. The solution can be computed using a shooting method according to the following steps:

1. Guess the value of $x_3(0) \equiv f''(\eta = 0)$.
2. Integrate equations (10.3.20) from $\eta = 0$ to $\eta = \infty$, subject to the initial conditions (10.3.16), using the value of $x_3(\eta = 0)$.
3. Check whether the far-field condition $x_3(\eta = \infty) = 1$ is satisfied. If not, improve the guess for $q(\eta = 0)$ and return to Step 2.

In practice, integrating up to $\eta = 10$ in Step 2 yields satisfactory accuracy. The improvement in Step 3 can be made using several methods.[1]

The following MATLAB code, entitled *blasius,* located in directory *10_bl* of FDLIB, performs the integration in the second step using the modified Euler (RK2) method:

```
%========
% Solution of the Blasius boundary-layer equation
%=======

Nstep = 64;     % integration steps
etamax = 10.0;
deta = etamax/Nstep;

eta = 0.0;
x(1) = 0.0; x(2) = 0.0; x(3) = 0.332;

xplot(1) = eta;
yplot1(1) = x(1);
yplot2(1) = x(2);
yplot3(1) = x(3);

%---
for i=2:Nstep+1

  xp = blasius_ode(x);

  for j=1:3
    xsave(j) = x(j);
    xpsave(j) = xp(j);
    x(j) = x(j) + xp(j)*deta;
  end

  eta = eta + deta;
  xp = blasius_ode(x);

  for j=1:3
    x(j) = xsave(j) + 0.5*(xpsave(j)+xp(j))*deta;
  end
```

---

[1] Pozrikidis, C. (2008) *Numerical Computation in Science and Engineering*, Second Edition, Oxford University Press.

```
  xplot(i) = eta;
  yplot1(i) = x(1); yplot2(i) = x(2); yplot3(i) = x(3);

end
%---

%---
% plotting
%---

hold on
plot(yplot1,xplot,'--')
plot(yplot2,xplot)
plot(yplot3,xplot,':')
ylabel('\eta','fontsize',15)
```

The program calls the following MATLAB function to evaluate the right-hand side of the differential equations:

```
function xp = blasius_ode(x)

%---
% Blasius odes
%---

  xp(1) = x(2);
  xp(2) = x(3);
  xp(3) = -0.50*x(1)*x(3);

end
```

This function receives the vector `x` in the input and generates the rate-of-change vector `xp` in the output.

Numerical computations show that the far-field boundary condition is satisfied when $f''(0) \simeq 0.332$, to shown precision. The corresponding profile of the streamwise velocity, $u/U = f' \equiv \mathrm{d}f/\mathrm{d}\eta$, is drawn with the solid line in Figure 10.3.2. The profiles of f and $f'' \equiv \mathrm{d}^2 f/\mathrm{d}\eta^2$ are drawn with the dashed and dotted lines.

The numerical solution shows that $u/U = 0.99$ when $\eta \simeq 4.9$, to shown precision. Based on this result, we may define the 99% boundary-layer thickness

$$\delta_{99} = 4.9\sqrt{\frac{\nu x}{U}} \qquad \text{or} \qquad \frac{\delta_{99}}{x} = 4.9\,\frac{1}{\mathrm{Re}_x}, \tag{10.3.22}$$

where $\mathrm{Re}_x \equiv Ux/\nu$ is the local Reynolds number. The 99.5% boundary-layer thickness is defined in a similar fashion. The numerical solution shows that the corresponding coefficient on the right-hand side of equations (10.3.22) is approximately equal to 5.3.

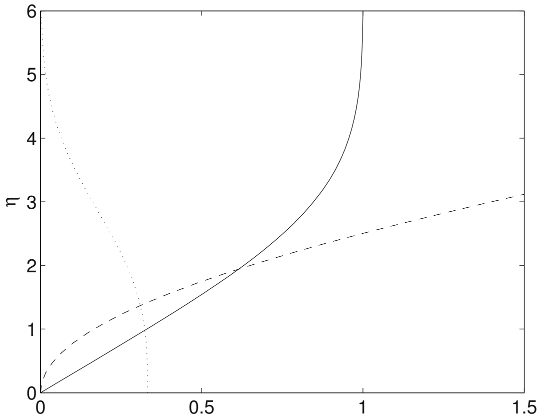

Figure 10.3.2 Profiles of the Blasius self-similar streamwise velocity, $u/U = f'$ (solid line) and its integral and derivative functions f and f'' (dashed and dotted lines).

10.3.3 Wall shear stress and drag force

The wall shear stress and drag force exerted on a boundary are of particular interest in the engineering design of equipment for high-speed flow. According to the Blasius similarity solution, the wall shear stress is given by

$$\tau_{xy}(x) = \mu \left(\frac{\partial u_x}{\partial y} \right)_{y=0} = \frac{f''(0)}{\sqrt{\mathrm{Re}_x}}\, \rho U^2 = 0.332\, \frac{1}{\sqrt{\mathrm{Re}_x}}\, \rho U^2. \qquad (10.3.23)$$

We observe that the wall shear stress takes an infinite value at the leading edge and decreases like the inverse square root of the streamwise distance or local Reynolds number, Re_x, along the plate. However, the physical significance of the singular behavior at the origin is compromised by the breakdown of the assumptions that led us to the boundary-layer equations at the leading edge.

Drag force

Even though the shear stress is infinite at the leading edge, the inverse-square-root singularity is integrable and the drag force exerted on any finite section of the plate extending from the leading edge up to an arbitrary point is finite. Using the similarity solution, we find that the drag force exerted on *both* sides of the plate over a length extending from the leading edge up to a certain distance x, is given by

$$D(x) \equiv 2 \int_0^x \tau_{xy}(\xi)\, \mathrm{d}\xi = 0.664\, \rho U \sqrt{U\nu} \int_0^x \frac{\mathrm{d}\xi}{\sqrt{\xi}}. \qquad (10.3.24)$$

Performing the integration, we obtain

$$D(x) = 1.328\, \frac{1}{\sqrt{\mathrm{Re}_x}}\, \rho U^2 x. \qquad (10.3.25)$$

Based on this expression, we define the dimensionless drag coefficient

$$\boxed{c_\mathrm{D} \equiv \frac{D}{\frac{1}{2}\rho U^2 x} = 2.656\,\frac{1}{\sqrt{\mathrm{Re}_x}}.} \tag{10.3.26}$$

The predictions of equations (10.3.25) and (10.3.26) agree with laboratory measurements up to about $\mathrm{Re}_x \simeq 1.2 \times 10^5$. Beyond that point, the flow inside the boundary layer develops a wavy pattern and ultimately becomes turbulent. Above the critical value of Re_x, the function $c_\mathrm{D}(\mathrm{Re}_x)$ jumps to a different branch with significantly higher values.

10.3.4 Vorticity transport

Neglecting the velocity component normal to the boundary layer, along the y axis, we find that the z component of the vorticity inside the boundary layer is given by

$$\omega_z(x,y) \simeq -\frac{\partial u_x}{\partial y} = -\frac{f''(\eta)}{\sqrt{\mathrm{Re}_x}}\,\frac{U^2}{\nu} = -f''(\eta)\,\frac{U}{\delta(x)}. \tag{10.3.27}$$

We observe that the strength of the vorticity at a particular location, η, decreases like the inverse of the local boundary-layer thickness, $\delta(x)$, due to the broadening of the velocity profile.

The streamwise rate of convection of vorticity across a plane that is perpendicular to the plate is given by

$$\int_0^\infty u_x(x,y)\,\omega_z(x,y)\,\mathrm{d}y \simeq -\int_0^\infty u_x(x,y)\,\frac{\partial u_x}{\partial y}\,\mathrm{d}y = -\tfrac{1}{2}\,U^2, \tag{10.3.28}$$

which is independent of the downstream position, x. Thus, the flux of vorticity across the plate is zero and viscous diffusion of vorticity does not occur at the wall, in agreement with our earlier observation that the gradient of the vorticity vanishes at the wall,

$$U\,\frac{\partial f'''}{\partial y} = \frac{\partial^2 u_x}{\partial y^2} = -\frac{\partial \omega}{\partial y} = 0. \tag{10.3.29}$$

Consequently, all convected vorticity is generated at the leading edge where the boundary-layer approximation ceases to be valid. Viscous stresses at the leading edge somehow generate the proper amount of vorticity necessary for the Blasius self-similar flow.

PROBLEMS

10.3.1 🖥 *Blasius solution*

Use the shooting method to compute $f''(0)$ for the Blasius boundary layer, accurate to the sixth decimal place.

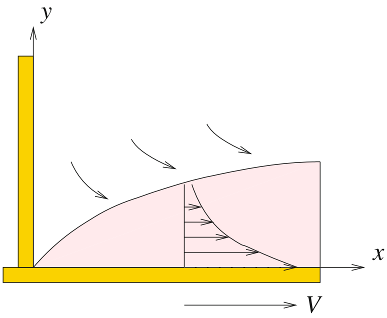

Figure 10.3.3 Illustration of the Sakiadis boundary layer developing over a semi-infinite translating belt.

10.3.2 *Sakiadis boundary layer*

Consider flow due to the translation of a semi-infinite belt along the x axis with velocity V normal to a vertical stationary wall, as illustrated in Figure 10.3.3. A boundary layer identified by Sakiadis is established along the belt.[2]

(a) Show that the flow in the boundary layer is governed by the Blasius equation (10.3.15), subject to the modified boundary conditions $f = 0$ and $f' = 0$ at $\eta = 0$, and $f' \to 0$ as η tends to infinity.

(b) Obtain the solution using the shooting method, plot the streamwise velocity profile, and discuss the structure of the flow field far from the moving belt. *Hint*: the iterations converge when $f''(0) = -0.44375$.

10.4 Displacement and momentum thickness

Because of the broadening of the velocity profile in the streamwise direction, x, the streamlines inside the Blasius boundary layer are deflected upward and away from the plate, as shown in Figure 10.3.1. To quantify this deflection, we introduce the displacement thickness.

Displacement thickness

Consider a streamline outside the boundary layer, described by the equation $y = g(x)$, and write a mass balance over a control area that is enclosed by (a) the streamline, (b) a vertical plane located at $x = 0$, (c) a vertical plane located at a certain distance x, and (d) the plate. Since the streamwise velocity profile at the leading edge located at $x = 0$ is flat, we obtain

$$\int_0^{g(0)} U \,\mathrm{d}y = \int_0^{g(x)} u_x(x, y) \,\mathrm{d}y. \tag{10.4.1}$$

---

[2] Sakiadis, B. C., (1961) Boundary-layer behavior on continuous solid surfaces: I. Boundary-layer equations for two-dimensional and axisymmetric flow, *AIChE J.* **7**, 26–28; II. The boundary layer on a continuous flat surface, *AIChE J.* **7**, 221–225.

Straightforward rearrangement yields the equation

$$U\left(g(x) - g(0)\right) = \int_0^{g(x)} \left(U - u_x(x,y)\right) \mathrm{d}y. \tag{10.4.2}$$

Taking the limit as the streamline under consideration moves increasingly far from the plate, we derive the equation

$$\lim_{x\to\infty} \left(g(x) - g(0)\right) = \delta^*(x), \tag{10.4.3}$$

where

$$\delta^*(x) \equiv \int_0^{\infty} \left(1 - \frac{u_x}{U}\right) \mathrm{d}y \tag{10.4.4}$$

is defined as the displacement thickness.

Using the numerical solution of the Blasius equation to evaluate the integral on the right-hand side of (10.4.4), we derive the exact relation

$$\delta^*(x) = \left(\frac{\nu x}{U}\right)^{1/2} \int_0^{\infty} \left(1 - \frac{\mathrm{d}f}{\mathrm{d}\eta}\right) \mathrm{d}\eta = 1.721 \sqrt{\frac{\nu x}{U}}, \tag{10.4.5}$$

which shows that the displacement thickness, like the 99% boundary-layer thickness, increases like the square root of the streamwise position, x.

Physically, the displacement thickness describes the vertical displacement of the streamlines far from from the plate with respect to their elevation at the leading edge. Laboratory experiments have shown that the boundary layer undergoes a transition from the laminar to the turbulent state when the displacement thickness reaches the approximate value $\delta^* \sim 600\,\nu/U$. At that point, turbulent shear stresses become significant and the analysis pursued in this section based on the assumption of laminar flow ceases to be valid.

The displacement thickness describes the surface of a fictitious impenetrable but slippery body that is held stationary in the incident irrotational flow. An improved boundary-layer theory can be developed by replacing the tangential velocity of the outer flow along the plate, U, with the corresponding tangential component of the velocity of the irrotational flow past the fictitious body. The irrotational flow past the fictitious body must be computed after the displacement thickness has been established, as discussed in this section. This iterative improvement provides us with a basis for describing the flow in the context of asymptotic expansions.

Momentum thickness

It is illuminating to perform a momentum integral balance over the control area used previously to define the displacement thickness. Since the upper boundary of the control volume is a streamline, it does not contribute to the rate of momentum input. Assuming that the normal stresses at the vertical sides are equal in magnitude and opposite in sign, which is justified by the assumption that the pressure drop across the boundary layer is negligibly small, and neglecting the traction along the top streamline, we obtain

$$\int_0^{g(0)} U\,(\rho\,U)\,\mathrm{d}y - \int_0^{g(x)} u_x\,(\rho\,u_x)\,\mathrm{d}y - \tfrac{1}{2}\,D(x) = 0, \tag{10.4.6}$$

where $D(x)$ is the drag force exerted on *both* sides of the plate, defined in equation (10.3.25). Now we make the upper limits of integration equal by recasting (10.4.6) into the form

$$-\rho\,U^2\,\big(\,g(x) - g(0)\,\big) - \rho\int_0^{g(x)} (U^2 - u_x^2)\,\mathrm{d}y - \tfrac{1}{2}\,D(x) = 0. \tag{10.4.7}$$

Finally, we take the limit as the streamline defining the top of the control area moves far from the plate, and use the definitions (10.4.3) and (10.4.4) to obtain the relation

$$D(x) = 2\,\rho\,U^2\Theta(x), \tag{10.4.8}$$

where Θ is the momentum thickness defined as

$$\Theta(x) \equiv \int_0^\infty \frac{u_x}{U}\,(1 - \frac{u_x}{U})\,\mathrm{d}y. \tag{10.4.9}$$

Using the numerical solution of the Blasius equation, we find that

$$\Theta(x) = \sqrt{\frac{\nu x}{U}}\int_0^\infty f'(\eta)\,\big(\,1 - f'(\eta)\,\big)\,\mathrm{d}\eta = 0.664\,\sqrt{\frac{\nu x}{U}}, \tag{10.4.10}$$

where $f'(\eta) = \mathrm{d}f/\mathrm{d}\eta$.

Shape factor

The ratio between the displacement and the momentum thickness is called the shape factor,

$$H \equiv \frac{\delta^*}{\Theta}. \tag{10.4.11}$$

Substituting the right-hand sides of expressions (10.4.5) and (10.4.9) into (10.4.11), we find that, for the boundary layer over a flat plate, $H = 2.591$.

Inspecting the definitions of δ^* and Θ, given in equations (10.4.4) and (10.4.8), we find that the shape factor is greater than unity as long as the streamwise velocity u_x is less than U inside a substantial portion of the boundary layer. The satisfaction of this constraint is consistent with physical intuition. The smaller the value of H, the more blunt the velocity profile across the boundary layer.

Relation between the wall shear stress and momentum thickness

The momentum thickness is related to the wall shear stress, and *vice versa*, by the integral momentum balance expressed by equation (10.4.8). Differentiating (10.3.25) with respect to x, we find that

$$\frac{\mathrm{d}D(x)}{\mathrm{d}x} = 2\,\tau_{xy}(x). \tag{10.4.12}$$

Expressing the drag force in terms of the momentum thickness using (10.4.8), we obtain

$$\tau_{xy}(x) = \rho U^2 \frac{\mathrm{d}\,\Theta(x)}{\mathrm{d}x}. \tag{10.4.13}$$

Thus, if the shear stress is known, the momentum thickness can be computed by integration. Conversely, if the momentum thickness is known, the shear stress can be computed by differentiation.

10.4.1 Von Kàrmàn's approximate method

Given the velocity profile across a boundary layer, we have two ways of computing the wall shear stress: directly by differentiation, and indirectly by evaluating the momentum thickness and then differentiating it with respect to streamwise position, x, to obtain the shear stress according to equation (10.4.13). The indirect method is less sensitive to the structure of the velocity profile near the wall. For the velocity profile that arises by solving the Blasius equation, the two methods are equivalent (Problem 10.4.1).

To implement the indirect method, we may introduce a self-similar velocity profile with some reasonable form involving an unspecified function that is either stipulated by physical intuition or suggested by laboratory observation. Our goal is to adjust the unspecified function so that the two methods of computing the wall shear stress discussed in the preceding paragraph are equivalent.

A reasonable velocity profile is

$$\frac{u_x}{U} = \frac{\mathrm{d}f(\eta)}{\mathrm{d}\eta} = \begin{cases} \sin \dfrac{\pi y}{2\,\Delta(x)} & \text{for } 0 < y < \Delta(x), \\ 1 & \text{for } y > \Delta(x), \end{cases} \tag{10.4.14}$$

where

$$\eta \equiv \frac{y}{\Delta(x)}, \tag{10.4.15}$$

and $\Delta(x)$ is an unspecified function playing the role of a boundary-layer thickness, similar to the δ_{99} thickness introduced in equation (10.3.22). Note that the velocity distribution (10.4.14) conforms with the required boundary conditions $f'(0) = 0$, $f'''(0) = 0$, and $f'(\infty) = 1$, but does not satisfy the Blasius equation; a prime denotes a derivative with respect to η.

Differentiating the profile (10.4.14) with respect to y, we obtain the wall shear stress

$$\tau_{xy}(x) = \frac{\pi}{2}\,\frac{\mu U}{\Delta(x)}. \tag{10.4.16}$$

The displacement thickness, momentum thicknesses, and shape factor defined in (10.4.4) and (10.4.8) are found to be

$$\delta^*(x) = (1 - \frac{2}{\pi})\,\Delta(x) = 0.363\,\Delta(x), \qquad \Theta(x) = (\frac{2}{\pi} - \frac{1}{2})\,\Delta(x) = 0.137\Delta(x). \tag{10.4.17}$$

The shape factor defined in (10.4.11) is found to be

$$H = 2.660. \tag{10.4.18}$$

It is reassuring to observe that the shape factor is remarkably close to that arising from the exact solution of the Blasius equation, $H = 2.591$.

Now substituting the expressions for the momentum thickness and wall shear stress into the integral momentum balance (10.4.13), we derive an ordinary differential equation for $\Delta(x)$,

$$\frac{\pi}{2}\,\frac{\mu U}{\Delta(x)} = 0.137\,\rho\,U^2\,\frac{\mathrm{d}\Delta(x)}{\mathrm{d}x}. \tag{10.4.19}$$

Rearranging and integrating with respect to x subject to the initial condition $\Delta = 0$ at $x = 0$, we find that

$$\Delta(x) = 4.80\,\sqrt{\frac{\nu x}{U}}. \tag{10.4.20}$$

Substituting this expression back into (10.4.16) and (10.4.17), we find that

$$\tau_{xy}(x) = \frac{0.327}{\sqrt{Re_x}}\,\rho\,U^2, \qquad \delta^*(x) = 1.743\,\sqrt{\frac{\nu x}{U}}, \qquad \Theta(x) = 0.665\,\sqrt{\frac{\nu x}{U}}. \tag{10.4.21}$$

These approximate expressions are in remarkable agreement with their exact counterparts shown in (10.3.23), (10.4.5), and (10.4.9).

However, this level of agreement is fortuitous and atypical of the accuracy of the approximate method (Problem 10.4.2).

PROBLEMS

10.4.1 *Wall shear stress*

Confirm that the wall shear stress computed directly by differentiating the velocity profile across the Blasius boundary layer is the same as that arising by differentiating the momentum thickness with respect to streamwise position, x, according to equation (10.4.13).

10.4.2 *Von Kàrmàn's method*

Assume that the velocity profile across the Blasius boundary layer is described by a hyperbolic tangent function

$$u_x = U\tanh\frac{y}{\Delta(x)}. \tag{10.4.22}$$

Show that the effective boundary-layer thickness, wall shear stress, displacement thickness, and momentum thicknesses are given by the right-hand sides of equations (10.4.20) and

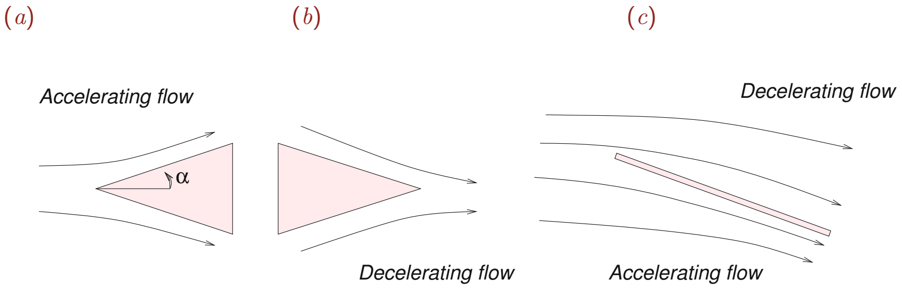

Figure 10.5.1 Boundary layers in accelerating or decelerating flow: (a, b) flow past a wedge and (c) uniform flow past a flat plate at a non-zero angle of attack.

(10.4.21), except that the numerical coefficients are equal, respectively, to 2.553, 0.392, 1.770, and 0.783. Discuss the accuracy of these results with reference to the exact solution.

10.4.3 💻 *Sakiadis' boundary layer*

Compute the displacement thickness, momentum thickness, and shape factor of the Sakiadis boundary layer discussed in Problem 10.3.2.

10.5 Boundary layers in accelerating or decelerating flow

In Section 10.3, we discussed the Blasius boundary layer developing along a flat plate parallel to a uniform incident streaming flow. One important feature of the parallel configuration is the uniformity of the tangential velocity of the outer flow over the plate. In this section, we consider the more general case of a Falkner–Skan boundary layer developing in an accelerating or decelerating incident flow. Examples of physical situations where such boundary layers occur are illustrated in Figure 10.5.1.

Consider an outer flow whose tangential velocity, $U_x(x)$, exhibits a power-law dependence on the streamwise distance from a specified origin, x, along a flat surface,

$$U_x(x) = c\,x^m, \tag{10.5.1}$$

where c is a positive coefficient and m is a positive or negative exponent. When $m = 0$, we recover the Blasius boundary layer over a flat plate at zero angle of attack. When $m = 1$, we obtain a boundary layer in orthogonal stagnation-point flow. Intermediate values of m correspond to symmetric flow past a wedge with semi-angle

$$\alpha = \frac{m}{m+1}\,\pi, \tag{10.5.2}$$

as illustrated in Figure 10.5.1(a). This expression can be inverted to give the exponent m in terms of α.

Differentiating (10.5.1) with respect to x, we obtain the streamwise acceleration or deceleration of the outer flow,

$$\frac{\mathrm{d}U_x}{\mathrm{d}x} = c\, m\, x^{m-1}. \tag{10.5.3}$$

Thus, the outer flow accelerates when $m > 0$ and decelerates when $m < 0$. In the first case, conservation of mass expressed by the continuity equation requires that the y derivative of the velocity component normal to the wall, U_y, is negative, $\partial U_y/\partial y < 0$. Since U_y is zero on the wall, it must be negative at the edge of the boundary layer. The associated motion of the outer fluid toward the wall confines the vorticity and reduces the thickness of the boundary layer with respect to that in a non-accelerating flow.

Substituting (10.5.3) into the boundary-layer equation (10.2.11) at steady state, we obtain the specific form

$$u_x \frac{\partial u_x}{\partial x} + u_y \frac{\partial u_x}{\partial y} = c^2 m\, x^{2m-1} + \nu \frac{\partial^2 u_x}{\partial y^2}. \tag{10.5.4}$$

Working as in Section 10.3 for the Blasius boundary layer, we identify the characteristic length L with the current streamwise position, x, and use (10.3.2) to define the boundary-layer thickness

$$\delta(x) \sim \sqrt{\frac{\nu\, x}{U_x(x)}} = \sqrt{\frac{\nu}{c\, x^{m-1}}}. \tag{10.5.5}$$

When $m = 1$, the boundary-layer thickness is constant, independent of x.

10.5.1 Self-similarity

We may assume that the velocity profile across the boundary is self-similar in x and y. The means that the scaled streamwise velocity profile, u_x/U_x, is a function of the dimensionless similarity variable

$$\eta \equiv \frac{y}{\delta(x)} = y\sqrt{\frac{U_x(x)}{\nu x}} = y\sqrt{\frac{c}{\nu x^{1-m}}}, \tag{10.5.6}$$

so that

$$u_x(x,y) = U_x(x)\, F(\eta), \tag{10.5.7}$$

where $F(\eta)$ is an *a priori* unknown function.

A key observation is that this self-similar profile can be derived from the stream function

$$\psi(x,y) = \sqrt{\nu\, U_x(x)\, x}\, f(\eta) = \sqrt{\nu\, c\, x^{m+1}}\, f(\eta), \tag{10.5.8}$$

where $F = \mathrm{d}f/\mathrm{d}\eta$, that is, F is the indefinite integral of f.

As a preliminary, we compute the derivatives

$$\frac{\partial\eta}{\partial x} = \frac{m-1}{2}\,\frac{y}{x}\sqrt{\frac{c\,x^{m-1}}{\nu}}, \qquad \frac{\partial\eta}{\partial y} = \sqrt{\frac{c}{\nu x^{1-m}}}. \tag{10.5.9}$$

Differentiating (10.5.5) with respect to x, we derive expressions for the two velocity components,

$$u_x(x,y) = \frac{\partial\psi}{\partial y} = U_x(x)\,\frac{\mathrm{d}f}{\mathrm{d}\eta} = c\,x^m\,\frac{\mathrm{d}f}{\mathrm{d}\eta} \tag{10.5.10}$$

and

$$u_y(x,y) = -\frac{\partial\psi}{\partial x} = \tfrac{1}{2}\,(\nu c x^{m-1})^{1/2}\,\Big(\,(1-m)\,\eta\,\frac{\mathrm{d}f}{\mathrm{d}\eta} - (1+m)\,f\,\Big). \tag{10.5.11}$$

Further differentiation yields

$$\frac{\partial u_x}{\partial x} = c\,m\,x^{m-1}\frac{\mathrm{d}f}{\mathrm{d}\eta} + U_x\,\frac{\mathrm{d}^2 f}{\mathrm{d}\eta^2}\,\frac{\partial\eta}{\partial x} \tag{10.5.12}$$

and

$$\frac{\partial u_x}{\partial y} = U_x\,\frac{\mathrm{d}^2 f}{\mathrm{d}\eta^2}\,\frac{\partial\eta}{\partial y}, \qquad \frac{\partial^2 u_x}{\partial y^2} = U_x\,\frac{\mathrm{d}^3 f}{\mathrm{d}\eta^3}\,\Big(\frac{\partial\eta}{\partial y}\Big)^2. \tag{10.5.13}$$

Substituting these expressions into the boundary-layer equation (10.5.4) and simplifying, we derive the Falkner–Skan ordinary differential equation for the function f,

$$\frac{\mathrm{d}^3 f}{\mathrm{d}\eta^3} + \tfrac{1}{2}\,(m+1)\,f\,\frac{\mathrm{d}^2 f}{\mathrm{d}\eta^2} - m\,\Big(\frac{\mathrm{d}f}{\mathrm{d}\eta}\Big)^2 + m = 0, \tag{10.5.14}$$

which is to be solved subject to the boundary conditions expressed by (10.3.16) and (10.3.17). When $m = 0$, we recover the Blasius equation (10.3.15). Since boundary conditions are specified at both ends of the solution domain $(0, \infty)$, we are presented with a two-point boundary-value problem involving three first-order differential equations.

10.5.2 Numerical solution

The boundary-value problem can be solved by the shooting method discussed in Section 10.3.2 for the Blasius equation. The counterpart of the Blasius system of first-order differential equations (10.3.20) is

$$\frac{\mathrm{d}x_1}{\mathrm{d}\eta} = x_2, \qquad \frac{\mathrm{d}x_2}{\mathrm{d}\eta} = x_3, \qquad \frac{\mathrm{d}x_3}{\mathrm{d}\eta} = -\tfrac{1}{2}\,(m+1)\,x_1\,x_3 + m\,x_2^2 - m. \tag{10.5.15}$$

The boundary conditions require that $x_1(\eta = 0) = 0$, $x_2(\eta = 0) = 0$, and $x_3(\eta = \infty) = 1$.

We find that convergence is achieved when $f''(0) = 1.491$ for $m = 1.5$, $f''(0) = 1.231$ for $m = 1.0$, $f''(0) = 0.675$ for $m = 0.25$, $f''(0) = 0.594$ for $m = 0.176$, $f''(0) = 0.332$ for $m = 0$, and $f''(0) = 0$ for $m = -0.0904$.

Streamwise velocity profiles expressed by the derivative $f'(\eta)$ are plotted in Figure 10.5.2 for several values of m. The profiles for $m < 0$, corresponding to decelerating flow, exhibit an inflection point near the wall. The wall shear stress vanishes when $m = -0.0904$.

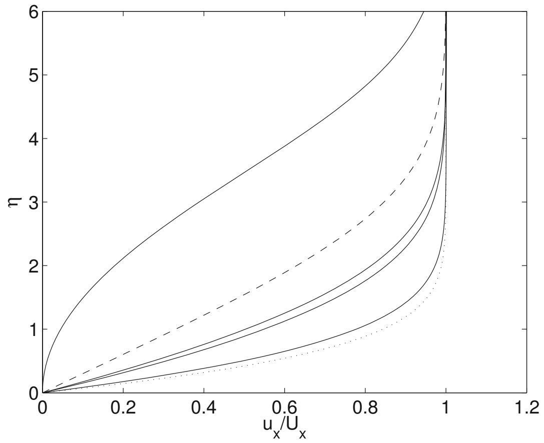

Figure 10.5.2 Velocity profiles across Falkner–Skan boundary layers for several values of the acceleration parameter m; from bottom to top, $m = 1.5$ (dotted line), 1.0, 0.25, 0.176, 0.0 (dashed line), and -0.0904.

PROBLEMS

10.5.1 *Orthogonal stagnation-point flow*

The Falkner–Skan profile with $m = 1$ corresponds to irrotational orthogonal stagnation-point flow against a flat plate.

(a) Derive the velocity field of the outer irrotational flow.

(b) Show that the Falkner–Skan boundary-layer solution satisfies the unsimplified Navier–Stokes equation, and thus it provides us with an exact solution.

10.5.2 💻 *Falkner–Skan equations*

Compute the velocity profile across a Falkner–Skan boundary layer with $m = -0.05$.

10.6 Momentum integral method

We have discussed the solution of the boundary-layer equations over a flat surface subject to a constant, accelerating, or decelerating outer flow with a power-law dependence on streamwise position. To compute boundary layers developing over curved surfaces and for more general types of outer flow, we resort to approximate methods.

Von Kàrmàn developed an elegant and efficient method for computing the flow inside a two-dimensional boundary layer developing over a surface with arbitrary shape, based on an integral momentum balance. The formulation culminates in an ordinary differential equation for a properly defined boundary-layer thickness with respect to arc length measured along the surface.

Flow over a flat surface

To illustrate the method, we consider the boundary layer developing over a flat surface located at $y = 0$, and introduce a control area confined between two vertical planes located at x_1 and x_2, the flat surface, and a horizontal plane located at the elevation $y = h$. Consistent with our previous notation, we denote the tangential component of the outer flow along the surface by $U_x(x)$. For simplicity, we assume that the physical properties of the fluid are uniform throughout the domain of flow.

We begin by considering the x component of the integral momentum balance (6.2.20), and introduce the Newtonian constitutive equation for the stress tensor. Neglecting the normal viscous stresses over the vertical and top planes, and assuming that gravitational effects are negligibly small, we obtain

$$\begin{aligned} &\int_{x_1}^{x_2}\int_0^h \rho\left(\frac{\partial u_x}{\partial t}\right)_{(x,y)} \mathrm{d}y\,\mathrm{d}x - \int_0^h [u_x\,(\rho\,u_x)]_{(x=x_1,y)}\,\mathrm{d}y \\ &\quad + \int_0^h [u_x\,(\rho\,u_x)]_{(x=x_2,y)}\,\mathrm{d}y + \int_{x_1}^{x_2} [u_y\,(\rho\,u_x)]_{(x,y=h)}\,\mathrm{d}x \\ &\quad = \int_0^h (-p)_{(x=x_1,y)}\,\mathrm{d}y - \int_0^h (-p)_{(x=x_2,y)}\,\mathrm{d}y - \int_{x_1}^{x_2} \tau_{xy}(x)\,\mathrm{d}x. \end{aligned} \tag{10.6.1}$$

Next, we take the limit as x_1 tends to x_2, recall that the pressure remains constant across the boundary layer, set $u_x(x, y = h) = U_x(x)$, and rearrange to obtain an integro-differential relation,

$$\begin{aligned} \rho\int_o^h \frac{\partial u_x}{\partial t}\,\mathrm{d}y = h\left(\frac{\partial p}{\partial x}\right)_{y=h} \\ -\rho\,\frac{\partial}{\partial x}\int_0^h u_x^2(x,y)\,\mathrm{d}y - \rho\,U_x(x)\,u_y(x,y=h) - \tau_{xy}(x). \end{aligned} \tag{10.6.2}$$

To reduce the number of unknowns, we eliminate $u_y(x, y = h)$ in favor of u_x using the continuity equation, setting

$$u_y(x,y=h) = -\int_0^h \frac{\partial u_x}{\partial x}(x,y')\,\mathrm{d}y'. \tag{10.6.3}$$

Moreover, we use the x component of Euler's equation (6.4.4) to evaluate the streamwise pressure gradient, finding that

$$\frac{\partial p}{\partial x} = -\rho\left(\frac{\partial U_x}{\partial t} + U_x\,\frac{\partial U_x}{\partial x}\right). \tag{10.6.4}$$

Substituting expressions (10.6.3) and (10.6.4) into (10.6.2) and rearranging, we obtain

$$\begin{aligned} \rho\int_o^h \frac{\partial(U_x - u_x)}{\partial t}\,\mathrm{d}y = -\rho\,\frac{\partial}{\partial x}\int_0^h u_x\,(U_x - u_x)\,\mathrm{d}y \\ -\rho\,\frac{\partial}{\partial x}\int_0^h U_x\,(U_x - u_x)\,\mathrm{d}y + \rho\,U_x\,\frac{\partial}{\partial x}\int_0^h (U_x - u_x)\,\mathrm{d}y + \tau_{xy}(x), \end{aligned} \tag{10.6.5}$$

which can be interpreted as an evolution equation for the momentum deficit expressed by the term $\rho\,(U_x - u_x)$.

Now we let the scaled height h/δ tend to infinity, and use the definitions of the displacement and momentum thickness stated in equations (10.4.4) and (10.4.9) to derive the von Kàrmàn integral momentum balance

$$\rho\,\frac{\partial(U_x\,\delta^*)}{\partial t} + \rho\,\frac{\partial(U_x^2\,\Theta)}{\partial x} + \rho\,\frac{\partial(U_x^2\,\delta^*)}{\partial x} - \rho\,U_x\,\frac{\partial(U_x\,\delta^*)}{\partial x} - \tau_{xy} = 0. \tag{10.6.6}$$

Rearranging, we derive an expression for the wall shear stress in terms of the displacement and momentum thickness,

$$\frac{\tau_{xy}}{\rho\,U_x^2} = \frac{\partial(U_x\delta^*)}{\partial t} + \frac{\partial\Theta}{\partial x} + (2\Theta + \delta^*)\,\frac{1}{U_x}\,\frac{\partial U_x}{\partial x}. \tag{10.6.7}$$

If the flow is steady, the first term on the right-hand side does not appear. It is reassuring to confirm that, when U_x is constant, equation (10.6.7) reduces to equation (10.4.13) describing the boundary layer developing over a flat plate that is held stationary parallel to an incident streaming flow.

If fluid is injected into the flow or withdrawn through a porous wall with normal velocity V, the right-hand side of (10.6.7) contains the additional term, $-V/U_x$, where V is positive in the case of injection and negative in the case of suction.

10.6.1 The von Kàrmàn–Pohlhausen method

Von Kàrmàn and Pohlhausen developed an approximate method for computing the boundary-layer thickness and associated structure of the flow based on the momentum integral balance (10.6.7). In the first state, we assume a sensible velocity profile across the boundary layer of the form $u_x = F(\eta)$, where $\eta \equiv y/\Delta(x)$ and $\Delta(x)$ is a boundary-layer thickness similar to the δ_{99} boundary layer thickness. In the second stage, we compute $\Delta(x)$ to satisfy the integral momentum balance equation (10.6.7).

The implementation of the method for flow over a flat plate at zero angle of attack where $F(\eta)$ is a quarter of a period of a sinusoidal function, as shown in (10.4.15), was discussed in Section 10.4. In the remainder of this section, we illustrate the implementation for an arbitrary steady flow.

10.6.2 Pohlhausen polynomials

Pohlhausen described the velocity profile across a boundary layer with a fourth-order polynomial,

$$\frac{u_x}{U_x} = F(\eta) = \begin{cases} a(x)\,\eta + b(x)\,\eta^2 + c(x)\,\eta^3 + d(x)\,\eta^4 & \text{for } 0 < \eta < 1, \\ 1 & \text{for } \eta > 1, \end{cases} \tag{10.6.8}$$

where $a(x), b(x), c(x)$, and $d(x)$ are position-dependent coefficients to be computed as part of the solution. Note that the functional form (10.6.8) satisfies the no-slip boundary condition at the wall corresponding to $\eta = 0$. To compute the four coefficients a, b, c, and d, we require four equations.

First, we require that the overall velocity profile is continuous and has a smooth first and second derivative at the edge of the boundary layer corresponding to $\eta = 1$, and thus obtain three conditions,

$$F = 1, \qquad \frac{\mathrm{d}F}{\mathrm{d}\eta} = 0, \qquad \frac{\mathrm{d}^2 F}{\mathrm{d}\eta^2} = 0 \tag{10.6.9}$$

at $\eta = 1$.

A fourth condition arises by applying the boundary-layer equation (10.2.5) at the wall located at $y = 0$, and then using the no-slip and no-penetration boundary conditions to set the left-hand side to zero. Evaluating the streamwise pressure gradient from (10.6.4) with the time derivative on the right-hand side set to zero, we find that

$$\left(\frac{\partial u_x^2}{\partial y^2}\right)_{y=0} = -\frac{1}{\nu}\, U_x\, \frac{\mathrm{d}U_x}{\mathrm{d}x}. \tag{10.6.10}$$

Next, we express the velocity in terms of the function $F(\eta)$ introduced in (10.6.8), and obtain

$$\left(\frac{\mathrm{d}^2 F}{\mathrm{d}\eta^2}\right)_{\eta=0} = -\Lambda, \tag{10.6.11}$$

where

$$\Lambda(x) \equiv \frac{\Delta^2(x)}{\nu}\, \frac{\mathrm{d}U_x}{\mathrm{d}x}, \tag{10.6.12}$$

is a dimensionless function expressing the ratio of the magnitude of the inertial acceleration forces in the outer irrotational flow to the magnitude of the viscous forces developing inside the boundary layer; if $\mathrm{d}U_x/\mathrm{d}x = 0$, then $\Lambda = 0$.

By definition, the effective boundary-layer thickness, $\Delta(x)$, is related to $\Lambda(x)$ by

$$\Delta(x) \equiv \sqrt{\frac{\nu\,\Lambda}{U_x'}}, \tag{10.6.13}$$

where $U_x' \equiv \mathrm{d}U_x/\mathrm{d}x$.

Requiring that the Pohlhausen profile (10.6.8) satisfies equations (10.6.9) and (10.6.11), we obtain

$$a = 2 + \tfrac{1}{6}\,\Lambda, \qquad b = -\tfrac{1}{2}\,\Lambda, \qquad c = -2 + \tfrac{1}{2}\,\Lambda, \qquad d = 1 - \frac{1}{6}\,\Lambda. \tag{10.6.14}$$

Substituting these expressions into (10.6.8) and rearranging, we obtain the velocity profile in terms of the parameter Λ,

$$\frac{u}{U_x} = F(\eta) = \begin{cases} \eta\,(2 - 2\,\eta^2 + \eta^3) + \Lambda\,\tfrac{1}{6}\,\eta\,(1-\eta)^3 & \text{for } 0 < \eta < 1, \\ 1 & \text{for } \eta > 1. \end{cases} \tag{10.6.15}$$

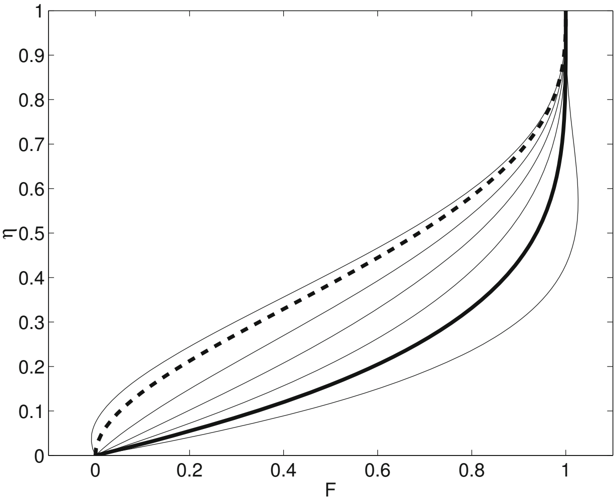

Figure 10.6.1 Profiles of Pohlhausen polynomials for $\Lambda = 20,\ 12$ (heavy solid line), $6,\ 0,\ -6,\ -12$ (heavy dashed line), and -15.

Program *pohl_pol*, located inside directory *10_bl* of FDLIB, computes polynomial profiles by evaluating the right-hand side of (10.6.15). A family of profiles is shown in Figure 10.6.1. The overshooting observed when $\Lambda > 12$, corresponding to a strongly accelerating external flow according to (10.6.12), places a limit on the physical relevance of the fourth-order polynomial expansion. When $\Lambda = -12$, the slope of the velocity profile is zero at the wall, and this suggests that the flow is on the verge of reversal. Under these conditions, the approximations that led us to the boundary-layer equations cease to be valid and the boundary layer is expected to separate from the wall and develop regions of recirculating fluid attached to the wall.

The displacement thickness, momentum thickness, and wall shear stress can be computed in terms of $\Delta(x)$ and $\Lambda(x)$ using the profiles (10.6.15), and are found to be

$$\delta^* = \frac{\Delta}{10}\,(3 - \tfrac{1}{12}\,\Lambda), \qquad \Theta = \frac{\Delta}{315}\,(37 - \tfrac{1}{3}\,\Lambda - \tfrac{5}{144}\,\Lambda^2), \tag{10.6.16}$$

and

$$\sigma_{xy}(x, y = 0) = \frac{\mu\,U_x}{\Delta}\,(2 + \tfrac{1}{6}\,\Lambda). \tag{10.6.17}$$

Expressing $\Delta(x)$ in terms of $\Lambda(x)$ using the definition (10.6.13), we obtain corresponding expressions in terms of Λ alone.

Next, we substitute the expressions given in (10.6.16) and (10.6.17) into the momentum integral balance (10.6.7), and thus derive a first-order nonlinear ordinary differential equation for $\Lambda(x)$ with respect to x. Having solved this equation, we recover the boundary-layer thickness, $\Delta(x)$, from the definition (10.6.13).

10.6.3 Numerical solution

It is convenient to introduce the Holstein–Bohlen parameter

$$\lambda(x) \equiv \frac{\Theta^2(x)}{\Delta^2(x)}\,\Lambda(x) = \frac{\Theta^2(x)}{\nu}\,\frac{\mathrm{d}U_x}{\mathrm{d}x}, \tag{10.6.18}$$

whose physical interpretation is similar to that of the parameter Λ discussed after the definition (10.6.12). Using the expression for the momentum thickness given in (10.6.16), we obtain a relationship between λ and Λ,

$$\lambda = \frac{\Lambda}{315^2}\,(37 - \frac{\Lambda}{3} - \tfrac{5}{144}\,\Lambda^2)^2. \tag{10.6.19}$$

The value $\Lambda = -12$ corresponds to $\lambda = -0.15673$ where the boundary layer is expected to separate, as shown in Figure 10.6.1.

To expedite the solution, we multiply both sides of the momentum integral balance (10.6.7) at steady state by Θ, and rearrange to obtain

$$\frac{\mathrm{d}}{\mathrm{d}x}\Big(\frac{\lambda}{\mathrm{d}U_x/\mathrm{d}x}\Big) \equiv \frac{1}{\nu}\,\frac{\mathrm{d}^2\Theta}{\mathrm{d}x^2} = 2\,\frac{S(\lambda) - [2 + H(\lambda)]\,\lambda}{U_x}, \tag{10.6.20}$$

where H is the shape factor defined in (10.4.11) and S is the shear function defined as

$$S(\lambda) \equiv \frac{\Theta}{\mu\,U_x}\,\sigma_{xy}(x, y = 0). \tag{10.6.21}$$

Physically, the shear function expresses the ratio of the wall shear stress to the average value of the shear stress across the boundary layer, and is thus another measure of the sharpness of the velocity profile across the boundary layer. Using the expressions given in (10.6.16) and (10.6.17), we find that

$$H = \frac{315}{10}\,\frac{3 - \frac{\Lambda}{12}}{37 - \frac{\Lambda}{3} - \frac{5}{144}\,\Lambda^2}, \qquad S = \frac{1}{315}\,(2 + \frac{\Lambda}{6})\,(37 - \frac{\Lambda}{3} - \tfrac{5}{144}\,\Lambda^2), \tag{10.6.22}$$

where Λ can be expressed in terms of λ using equation (10.6.19). The numerical procedure involves the following steps:

1. Given the value of λ at a particular position, x, compute the corresponding value of Λ by solving the nonlinear algebraic equation (10.6.19).
2. Evaluate the functions S and H using expressions (10.6.22).
3. Compute the right-hand side of (10.6.20) to obtain the rate of change of the ratio on the left-hand side with respect to x.
4. Advance the value of λ over a small increment, Δx.
5. Return to Step 1 and repeat the calculations for another cycle.

The following MATLAB function entitled *Lam* solves the nonlinear equation (10.6.19) required in Step 1 using Newton's method:

```
function Lam = root(lam,Lam)

%---
% given lambda, solve for Lambda
%---

if(abs(lam)<0.000005)
  Lam = 0.00001; return
end

%---
% Newton's method
%---

for i=1:50
  fnc = ltoL(lam,Lam);
  fnc1 = ltoL(lam,Lam+0.0001);
  fncp = (fnc1-fnc)/0.0001;
  corr = -fnc/fncp;
  Lam = Lam+corr;
  if(abs(corr)<0.000001) return; end
end

  disp 'root: could not find a root in 50 iterations'

return

%--------------

function f = ltoL(lam,Lam)

  f = Lam*((37.0-Lam/3.0-5.0*Lam*Lam/144.0)/315.0)^2-lam;

return
```

Note that the main function *Lam* is accompanied by an evaluator function *ltoL* (λ to Λ).

Evaluation at a stagnation point

The numerical integration typically begins at a stagnation point where the tangential velocity U_x vanishes and the right-hand side of (10.6.20) is undefined. To prevent a singularity, we require that the numerator is zero at that point, and thus obtain a nonlinear algebraic equation for Λ. A physically acceptable solution is $\Lambda = 7.0523231$, corresponding to $\lambda = 0.0770356$. These values are used to initialize the computation.

To evaluate the right-hand side of (10.6.20) at a stagnation point located at $x = 0$, we denote the expression enclosed by the pointed brackets on the right-hand side by $Q(\lambda)$. Applying the l'Hôspital rule to evaluate the fraction, we find that

$$\frac{\mathrm{d}}{\mathrm{d}x}\Big(\frac{\lambda}{\mathrm{d}U_x/\mathrm{d}x}\Big)_{x=0} = \Big(\frac{\mathrm{d}Q/\mathrm{d}x}{\mathrm{d}U_x/\mathrm{d}x}\Big)_{x=0} = \Big(\frac{\mathrm{d}Q/\mathrm{d}\lambda}{\mathrm{d}U_x/\mathrm{d}x}\,\frac{\mathrm{d}\lambda}{\mathrm{d}x}\Big)_{x=0} \tag{10.6.23}$$

and then

$$\frac{\mathrm{d}}{\mathrm{d}x}\Big(\frac{\lambda}{\mathrm{d}U_x/\mathrm{d}x}\Big)_{x=0} = \Big(\frac{\mathrm{d}Q}{\mathrm{d}\lambda}\Big)_{x=0}\Big(\frac{\mathrm{d}}{\mathrm{d}x}\big(\frac{\lambda}{\mathrm{d}U_x/\mathrm{d}x}\big) + \lambda\,\frac{\mathrm{d}^2U_x/\mathrm{d}x^2}{(\mathrm{d}U_x/\mathrm{d}x)^2}\Big)_{x=0}. \tag{10.6.24}$$

Combining the left-hand side with the first term inside the tall parentheses on the right-hand side, we obtain

$$\frac{\mathrm{d}}{\mathrm{d}x}\Big(\frac{\lambda}{\mathrm{d}U_x/\mathrm{d}x}\Big)_{x=0} = \Big(\frac{\lambda}{1-\mathrm{d}Q/\mathrm{d}\lambda}\,\frac{\mathrm{d}Q}{\mathrm{d}\lambda}\,\frac{\mathrm{d}^2U_x/\mathrm{d}x^2}{(\mathrm{d}U_x/\mathrm{d}x)^2}\Big)_{x=0}. \tag{10.6.25}$$

Evaluating the expression on the right-hand side using the definition of $Q(\lambda)$, we obtain the required initial value

$$\frac{\mathrm{d}}{\mathrm{d}x}\Big(\frac{\lambda}{\mathrm{d}U_x/\mathrm{d}x}\Big)_{x=0} = -0.0652\Big(\frac{\mathrm{d}^2U_x/\mathrm{d}x^2}{(\mathrm{d}U_x/\mathrm{d}x)^2}\Big)_{x=0}. \tag{10.6.26}$$

10.6.4 Boundary layer around a curved body

The Kàrmàn-Pohlhausen method was developed with reference to a planar boundary where the x coordinate increases along the boundary in the direction of the velocity of the outer flow. To tackle the more general case of a curved boundary, we replace x with the arc length along the boundary, ℓ, measured in the direction of the tangential velocity of the incident flow, and begin the integration from a stagnation point.

A difficulty arises at the critical point where the acceleration $\mathrm{d}U_\ell/\mathrm{d}\ell$ becomes zero or infinite. However, the ambiguity can be removed by carrying out the integration at that point using the Falkner–Skan similarity solution with a proper value for the exponent m.

Boundary layer around a circular cylinder

As an application, we consider streaming (uniform) flow past a stationary circular cylinder of radius a with vanishing circulation around the cylinder, as shown in Figure 10.6.2. Far from the cylinder, the flow is streaming toward the negative direction of the x axis and the velocity tends to the uniform value $-U\,\mathbf{e}_x$, where $U > 0$ is the magnitude of the streaming flow and $\mathbf{e}_x$ is the unit vector along the x axis.

Using the velocity potential for irrotational flow past a circular cylinder, given in equation (3.5.48) with $V_x = -U$, we find that the tangential component of velocity of the outer flow is

$$U_\theta(\theta) = \Big(\frac{\partial\phi}{\partial\theta}\Big)_{r=a} = 2\,U\sin\theta, \tag{10.6.27}$$

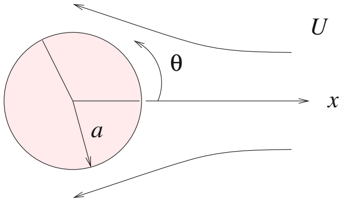

Figure 10.6.2 Illustration of the Prandtl boundary layer around a circular cylinder of radius a held stationary in an incident streaming flow with velocity U.

where θ is the polar angle measured around the center of the cylinder in the counterclockwise direction, as shown in Figure 10.6.2. The arc length around the cylinder measured from the front stagnation point is $\ell = a\theta$. The required derivatives of the velocity with respect to arc length are

$$\frac{\mathrm{d}U_\theta}{\mathrm{d}\ell} = \frac{1}{a}\,\frac{\mathrm{d}U_\theta}{\mathrm{d}\theta} = 2\,\frac{U}{a}\,\cos\theta, \qquad \frac{\mathrm{d}^2U_\theta}{\mathrm{d}\ell^2} = \frac{1}{a^2}\,\frac{\mathrm{d}^2U_\theta}{\mathrm{d}\theta^2} = -2\,\frac{U}{a^2}\,\sin\theta. \tag{10.6.28}$$

Equation (10.6.26) yields

$$\frac{\mathrm{d}}{\mathrm{d}\ell}\Big(\frac{\lambda}{\mathrm{d}U_\theta/\mathrm{d}\ell}\Big)_{\ell=0} = 0, \tag{10.6.29}$$

which is used to start up the computations.

The following MATLAB function named *phase_vel* evaluates the right-hand side of (10.6.20):

```
function f = phase_vel (U0,theta,Lam,lam)

  tmp = 37.0-Lam/3.0-5.0*Lam*Lam/144.0;
  H = 31.5*(3.0-Lam/12.0)/tmp;
  S = (2.0+Lam/6.0)*tmp/315.0;
  U = 2.0*U0*sin(theta);
  f = 2.0*(S-(2.0+H)*lam)/U;

return
```

The Kàrmàn-Pohlhausen method is implemented in the following MATLAB code entitled *kp_cc*, located in directory *10_bl* of FDLIB:

```
a = 1.0;   % cylinder radius
U0 = 1.0;   % incident velocity
nu = 1.0;   % kinematic viscosity
mu = 1.0;   % viscosity

Ndiv = 2*128;   % number of divisions
angle = 0.60*pi;   % maximum integration angle
```

```
%---
% prepare
%---

Dtht = angle/Ndiv;   % differential angle theta
Dx = a*Dtht;   % differential arc length

%---
% initial values
%---

tht = 0.0;
lam = 0.0770;
Lam = 7.052;
Up = 2.0*U0*cos(tht)/a;
z = lam/Up;

%---
% integrate by the modified Euler method
%---

for i=1:Ndiv

  U = 2.0*U0*sin(tht);   % velocity
  Up = 2.0*U0*cos(tht)/a;   % acceleration
  tmp = 37.0-Lam/3.0-5.0*Lam*Lam/144.0;
  H = 31.5*(3.0-Lam/12.0)/tmp;
  S = (2.0+Lam/6.0)*tmp/315.0;
  Del = sqrt(abs(nu*Lam/Up));
  del = Del*(3.0-Lam/12.0)/10.0;
  sw = mu*U/Del*(2.0+Lam/6.0);
  THeta = 0.0;

  if(abs(sw)>0.0000001)
    THeta = mu*U*S/sw;
  end

  if(i==1)
    fv = 0.0;
  else
    Lam = root(lam,Lam);
    fv = phase_vel(U0,tht,Lam,lam);
  end

  zsave = z;
fvsave = fv;
  tht = tht+Dtht;
  z = z + fv*Dx;
  Up = 2.0*U0*cos(tht)/a;
```

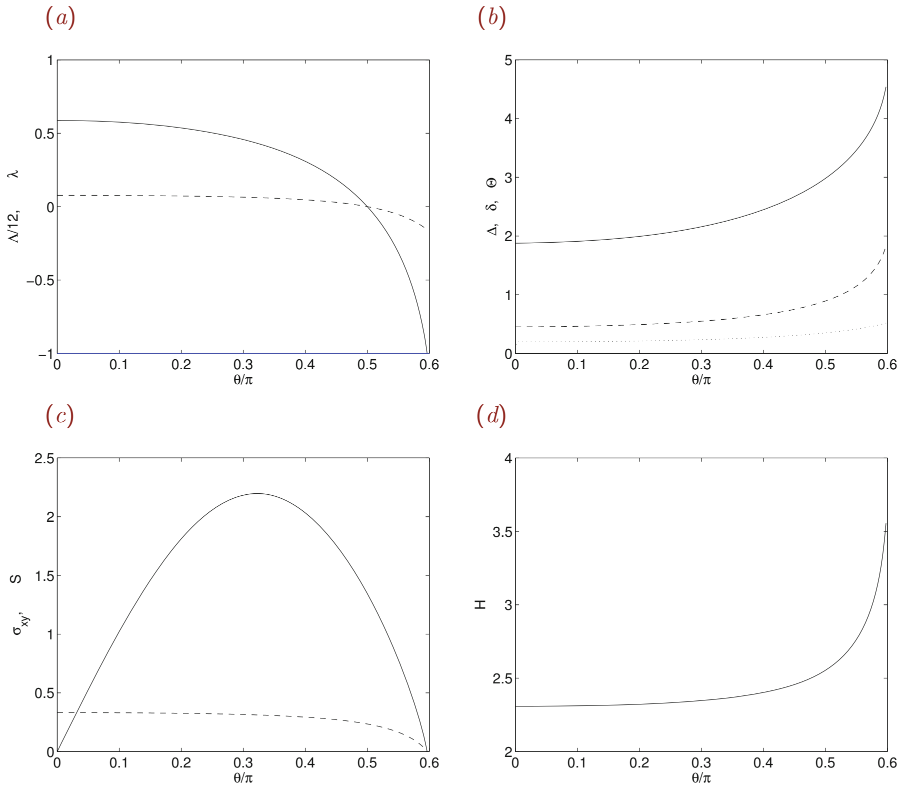

Figure 10.6.3 Features of the Prandtl boundary layer around a circular cylinder of radius a held stationary in an incident streaming flow with velocity U, computed by the von Kàrmàn-Pohlhausen method. (a) Distribution of the dimensionless parameters $\frac{1}{12}\,\Lambda$ (solid line) and λ (dashed line). (b) Boundary-layer thickness Δ (solid line), displacement thickness δ^* (dashed line), and momentum thickness Θ (dotted line); all are scaled by $\sqrt{\nu\, a/U}$. (c) Distribution of the wall shear stress scaled by $\mu\, U/a$ (solid line), and shape factor S (dashed line). (d) Distribution of the shear function, H.

```
  lam = z*Up;
  Lam = root(lam,Lam);   % solve for Lambda
  fv = phase_vel(U0,tht,Lam,lam);
  z = zsave + 0.5*(fv+fvsave)*Dx;
  lam = z*Up;

end
```

Graphs of the solution are shown in Figure 10.6.3. The velocity profile across the boundary layer at different stations around the cylinder can be inferred from the scaled Pohlhausen profiles shown in Figure 10.6.1 using the local value of Λ.

The numerical solution reveals that $\Lambda = -12$ when $\theta = 109.5°$. At that point, the shear stress becomes zero and the boundary layer is expected to separate. Comparing this result with the experimentally observed value $\theta = 80.5°$, we find a serious disagreement attributed to the deviation of the actual outer flow from the idealized potential flow distribution described by (10.6.27) due to the presence of a wake.

To improve the solution, we may describe the tangential velocity distribution U_θ by interpolation based on data collected in the laboratory. When this is done, the predictions of the boundary-layer analysis are in excellent agreement with laboratory observation.

PROBLEMS

10.6.1 *Von Kàrmàn method for the Blasius boundary layer*

Assume that the velocity profile across the Blasius boundary layer is given by the Pohlhausen polynomial (10.6.15). Show that the effective boundary-layer thickness, wall shear stress, displacement thickness, and momentum thicknesses are given by the right-hand sides of equations (10.4.20) and (10.4.21), except that the numerical coefficients are equal, respectively, to 5.863, 0.343, 1.751, and 0.685. Discuss the accuracy of these results with reference to the exact solution obtained by numerical methods.

10.6.2 💻 *Boundary layer around a circular cylinder*

Plot and discuss scaled velocity profiles u_θ/U_0 across the boundary layer around a circular cylinder at a sequence of angles, θ.

10.7 Instability of shear flows

In Chapter 7, we derived exact solutions of the governing equations for channel and tube flow, assuming unidirectional motion with rectilinear or circular streamlines. The physical relevance of these assumptions is corroborated by laboratory observations at low and moderate Reynolds numbers. However, at high Reynolds numbers, small perturbations inherent in any real flow amplify to initiate an unsteady motion, possibly leading to a new steady state that is different than that computed under the assumption of unidirectional flow.

Linear stability analysis

Two questions naturally arise: what is the threshold Reynolds number above which a flow becomes unstable? and what are the salient modes of amplification? To develop insight into the answers, we carry out a linear stability analysis. Our general strategy is to consider a flow of interest at steady state, introduce small perturbations, and describe the time evolution of the perturbations by solving simplified versions of the governing equations that arise by linearization. If all perturbations decay, the flow is stable; if some perturbations amplify, the flow is unstable; if some perturbations stay constant in time and all other perturbations decay, the flow is neutrally stable. Perturbations that grow or decay exponentially in time represent normal modes.

10.7.1 Stability analysis of shear flow

To illustrate the procedures, we consider a steady unidirectional flow along the x axis with velocity, pressure, and vorticity given by

$$u_x^{\mathrm{B}} = U(y), \qquad u_y^{\mathrm{B}} = 0, \qquad p^{\mathrm{B}} = -\chi\, x, \qquad \omega_z^{\mathrm{B}} = -\frac{\mathrm{d}U(y)}{\mathrm{d}y}, \tag{10.7.1}$$

where the superscript B designates the base flow whose stability is examined, $U(y)$ is the unperturbed velocity profile, and χ is the negative of the streamwise pressure gradient.

It should be noted that, unless the velocity profile is parabolic, the base flow will not satisfy the steady version of the equation of motion. However, we assume that the base flow evolves at a rate that is much slower than that of the perturbations, and may thus be considered to be in a quasi-steady state.

Perturbations and disturbances

Next, we introduce a two-dimensional perturbation whose velocity and pressure fields are described by

$$u_x^{\mathrm{P}}(x,y,t) = \epsilon\, u_x^{\mathrm{D}}(x,y,t), \qquad u_y^{\mathrm{P}}(x,y,t) = \epsilon\, u_y^{\mathrm{D}}(x,y,t),$$
$$p^{\mathrm{P}}(x,y,t) = \epsilon\, p^{\mathrm{D}}(x,y,t), \tag{10.7.2}$$

where the superscript P designates the perturbation, the superscript D designates the disturbance, and ϵ is a dimensionless coefficient whose magnitude is much smaller than unity. The corresponding perturbation in the vorticity is

$$\omega_z^{\mathrm{P}}(x,y,t) = \epsilon\, \omega^{\mathrm{D}}(x,y,t) = \epsilon\, \Big(\frac{\partial u_y^{\mathrm{D}}}{\partial x} - \frac{\partial u_x^{\mathrm{D}}}{\partial y} \Big)(x,y,t). \tag{10.7.3}$$

The physical flow arises by adding corresponding variables of the base and perturbation flows shown in (10.7.1) and (10.7.2). For example, the x velocity component of the perturbed flow is given by

$$u_x(x,y,t) = u_x^{\mathrm{B}}(y) + \epsilon\, u_x^{\mathrm{D}}(x,y,t). \tag{10.7.4}$$

Substituting this sum and its counterparts for other variables into the vorticity transport equation for two-dimensional flow stated in equation (6.6.14), we obtain

$$\epsilon\, \frac{\partial \omega_z^{\mathrm{D}}}{\partial t} + \epsilon\, u_x^{\mathrm{B}}\, \frac{\partial \omega_z^{\mathrm{D}}}{\partial x} + \epsilon^2\, u_x^{\mathrm{D}}\, \frac{\partial \omega_z^{\mathrm{D}}}{\partial x} + \epsilon\, u_y^{\mathrm{D}}\, \frac{\partial \omega_z^{\mathrm{B}}}{\partial y} + \epsilon^2\, u_y^{\mathrm{D}}\, \frac{\partial \omega_z^{\mathrm{D}}}{\partial y}$$
$$= \nu\, \Big(\frac{\partial^2 \omega^{\mathrm{B}}}{\partial x^2} + \frac{\partial^2 \omega^{\mathrm{B}}}{\partial y^2} + \epsilon\, \Big(\frac{\partial^2 \omega^{\mathrm{D}}}{\partial x^2} + \frac{\partial^2 \omega^{\mathrm{D}}}{\partial y^2} \Big) \Big), \tag{10.7.5}$$

where ν is the kinematic viscosity of the fluid. Since the vorticity of the base flow satisfies the steady version of the vorticity transport equation for unidirectional flow under the quasi-steady approximation, the sum of the first two terms on the right-hand side is zero.

Linearization

Because ϵ has been assumed small, quadratic terms that are proportional to ϵ^2 are small compared to linear terms that are proportional to ϵ, and may be discarded from both sides of (10.7.5). Collecting the linear terms and setting their sum to zero, we obtain the linearized vorticity transport equation

$$\frac{\partial \omega_z^{\mathrm{D}}}{\partial t} + u_x^{\mathrm{B}} \frac{\partial \omega_z^{\mathrm{D}}}{\partial x} + u_y^{\mathrm{D}} \frac{\partial \omega_z^{\mathrm{B}}}{\partial y} = \nu \left(\frac{\partial^2 \omega_z^{\mathrm{D}}}{\partial x^2} + \frac{\partial^2 \omega_z^{\mathrm{D}}}{\partial y^2} \right). \tag{10.7.6}$$

Substituting the expressions for the base flow stated (10.7.1) into (10.7.6), we derive the more specific form

$$\frac{\partial \omega_z^{\mathrm{D}}}{\partial t} + U(y) \frac{\partial \omega_z^{\mathrm{D}}}{\partial x} - u_y^{\mathrm{D}} \frac{\mathrm{d}^2 U}{\mathrm{d}y^2} = \nu \left(\frac{\partial^2 \omega_z^{\mathrm{D}}}{\partial x^2} + \frac{\partial^2 \omega_z^{\mathrm{D}}}{\partial y^2} \right). \tag{10.7.7}$$

The problem has been reduced to solving the linear equation (10.7.7) for the disturbance flow, subject to a specified initial condition and appropriate boundary conditions.

Disturbance stream function

It is convenient to express the disturbance flow in terms of a disturbance stream function, $\psi^{\mathrm{D}}(x, y, t)$, defined by the equations

$$u_x^D = \frac{\partial \psi^{\mathrm{D}}}{\partial y}, \qquad u_y^D = -\frac{\partial \psi^{\mathrm{D}}}{\partial x}. \tag{10.7.8}$$

The disturbance vorticity is given by

$$\omega_z^{\mathrm{D}} = -\left(\frac{\partial^2 \psi^{\mathrm{D}}}{\partial x^2} + \frac{\partial^2 \psi^{\mathrm{D}}}{\partial y^2} \right) = -\nabla^2 \psi^{\mathrm{D}}, \tag{10.7.9}$$

where $\nabla^2 \equiv \partial^2/\partial x^2 + \partial^2/\partial y^2$ is the Laplacian operator in the xy plane. Substituting these expressions into (10.7.7) and rearranging, we obtain

$$\frac{\partial\, \nabla^2 \psi^{\mathrm{D}}}{\partial t} + U(y) \frac{\partial\, \nabla^2 \psi^{\mathrm{D}}}{\partial x} - \nu\, \nabla^4\, \psi^{\mathrm{D}} = \frac{\partial \psi^{\mathrm{D}}}{\partial x} \frac{\mathrm{d}^2 U}{\mathrm{d}y^2}, \tag{10.7.10}$$

where $\nabla^4 = \nabla^2 \nabla^2$ is the biharmonic operator in the xy plane.

10.7.2 Normal-mode analysis

To study the evolution of each and every possible disturbance is practically impossible. To make progress, we exploit the linearity of equation (10.7.10) and deduce the nature of the general solution corresponding to an arbitrary initial condition from the behavior of an infinite family of solutions corresponding to disturbances that are sinusoidal functions of the streamwise position, x, and exponential functions of time, t, called normal modes. The general solution can be constructed by linear superposition.

Consider a normal mode with wave length L and corresponding wave number $k = 2\pi/L$. The disturbance stream function is expressed in the form

$$\psi^{\rm D}(x, y, t) = \chi_{\rm R}(y, t)\, \cos(kx) + \chi_{\rm I}(y, t)\, \sin(kx), \tag{10.7.11}$$

where $\chi_{\rm R}(y, t)$ and $\chi_{\rm I}(y, t)$ are two real functions. To simplify the notation, we introduce the complex function

$$\chi(y, t) \equiv \chi_{\rm R}(y, t) - {\rm i}\, \chi_{\rm I}(y, t), \tag{10.7.12}$$

where i is the imaginary unit, $\mathrm{i}^2 = -1$. Using the Euler decomposition of the imaginary exponential,

$$\exp(ikx) = \cos(kx) + {\rm i}\, \sin(kx), \tag{10.7.13}$$

we recast (10.7.11) into the form

$$\psi^{\rm D}(x, y, t) = {\rm real}\{\Psi^{\rm D}(x, y, t)\}, \tag{10.7.14}$$

where *real* designates the real part of the complex quantity enclosed by the angular brackets, and

$$\Psi^{\rm D}(x, y, t) \equiv \phi(y, t)\, \exp({\rm i}kx) \tag{10.7.15}$$

is a complex stream function. To simplify the analysis, we require that the imaginary part of $\Psi^{\rm D}$ also satisfies equation (10.7.10).

Substituting (10.7.15) into (10.7.10), carrying out the differentiation with respect to x, and noting that

$$\nabla^2 \Psi^{\rm D} = \big(-k^2 \phi + \frac{\partial^2 \phi}{\partial y^2} \big)\, \exp({\rm i}kx), \tag{10.7.16}$$

we derive the equation

$$-k^2 \frac{\partial \phi}{\partial t} + \frac{\partial^3 \phi}{\partial y^2\, \partial t} + {\rm i}\, k\, U(y)\, \big(-k^2 \phi + \frac{\partial^2 \phi}{\partial y^2} \big) \\ -\nu\, \big(k^4 \phi - 2k^2 \frac{\partial^2 \phi}{\partial y^2} + \frac{\partial^4 \phi}{\partial y^4} \big) = {\rm i}\, k\, \phi\, \frac{{\rm d}^2 U}{{\rm d}y^2}, \tag{10.7.17}$$

which should be regarded as a linearized vorticity transport equation.

Growth rate

A solution of (10.7.17) can be found by expressing $\phi(x, t)$ in the separated form

$$\phi(y, t) = f(y)\, \exp(-{\rm i}\, \sigma\, t) = f(y)\, \exp(-{\rm i}kct), \tag{10.7.18}$$

where $f(y)$ is a complex function, σ is a complex constant called the complex growth rate, and $c \equiv \sigma/k$ is another complex constant called the complex phase velocity.

Substituting (10.7.18) into (10.7.15), we derive the corresponding complex disturbance stream function

$$\Psi(x,y,t) = f(y)\,\exp[\,\mathrm{i}\,(kx-\sigma t)\,] = f(y)\,\exp[\,\mathrm{i}k(x-ct)\,]. \tag{10.7.19}$$

Next, we decompose σ and c into their real and imaginary parts, writing

$$\sigma = \sigma_{\mathrm{R}} + \mathrm{i}\,\sigma_{\mathrm{I}}, \qquad c = c_{\mathrm{R}} + \mathrm{i}\,c_{\mathrm{I}}, \tag{10.7.20}$$

and obtain the expression

$$\Psi(x,y,t) = f(y)\,\exp[\mathrm{i}\,k\,(x-c_{\mathrm{R}}t)]\,\exp(\sigma_{\mathrm{I}}t), \tag{10.7.21}$$

where the subscripts R and I stand for real and imaginary. Expression (10.7.21) illustrates two important features:

- The constant c_{R} is the real phase velocity of the disturbance. The crests and troughs of the sinusoidal perturbation, but not the fluid itself, travel along the x axis with velocity c_{R}.
- The constant $\sigma_{\mathrm{I}} = kc_I$ is the growth rate of the disturbance; if σ_{I} is positive, the disturbance grows at an exponential rate in time; if σ_{I} is negative, the disturbance decays at an exponential rate in time; if $\sigma_{\mathrm{I}} = 0$, the amplitude of the disturbance remains constant in time. In the first case, the flow is unstable; in the second case, the flow is stable; and in the third case, the flow is neutrally stable.

Orr–Sommerfeld equation

Substituting expression (10.7.18) into the governing equation (10.7.17), and rearranging the resulting expression, we derive the Orr–Sommerfeld equation,

$$k^4 f - 2\,k^2\,\frac{\mathrm{d}^2 f}{\mathrm{d}y^2} + \frac{\mathrm{d}^4 f}{\mathrm{d}y^4} = \frac{\mathrm{i}\,k}{\nu}\,\Big(\big(U(y)-c\big)\big(\frac{\mathrm{d}^2 f}{\mathrm{d}y^2} - k^2 f\big) - \frac{\mathrm{d}^2 U}{\mathrm{d}y^2}\,f\Big), \tag{10.7.22}$$

which can be classified as a linear ordinary differential equation with variable coefficients determined by the velocity profile. A trivial solution is $f = 0$.

Nontrivial solutions expressing normal modes are possible only for certain values of c that are the eigenvalues of the Orr–Sommerfeld equation. The main objective of linear stability analysis is to identify these eigenvalues and associated eigenfunctions, and thereby assess whether the amplitude of a normal mode will grow, decay, or remain constant in time.

Rayleigh equation

When viscous forces are negligible, the left-hand side of the Orr–Sommerfeld equation (10.7.22) may be set equal to zero, yielding the Rayleigh equation

$$\big(U(y)-c\big)\big(\frac{\mathrm{d}^2 f}{\mathrm{d}y^2} - k^2 f\big) - \frac{\mathrm{d}^2 U}{\mathrm{d}y^2}\,f = 0, \tag{10.7.23}$$

which is also available in the alternative form

$$\frac{\mathrm{d}^2 f}{\mathrm{d}y^2} - \Big(k^2 + \frac{1}{U(y) - c}\,\frac{\mathrm{d}^2 U}{\mathrm{d}y^2} \Big) f = 0. \tag{10.7.24}$$

Because of the absence of viscous forces, the Rayleigh equation is a second-order differential equation, whereas its inclusive Orr-Sommerfeld equation is a fourth-order differential equation. Both equations are linear, but the coefficients multiplying the derivatives of the unknown complex function f are not necessarily constant.

Numerical methods

Analytical solutions to the Orr–Sommerfeld and Rayleigh equations are possible only for a limited class of purely viscous or idealized inviscid flows. To study the stability of more general flows, we resort to numerical methods. Typical methods are discussed in Sections 10.8 and 10.9.

PROBLEM

10.7.1 *Instability of an inviscid shear flow*

Consider an infinite shear flow with velocity profile $U(y) = U_0 \tanh\eta$, where $\eta = y/\delta$ and δ is a specified length. Confirm that an eigenvalue and the corresponding eigenfunction of Rayleigh's equation describing a neutrally stable perturbation are $c = 0$ and $f(y) = A\,\mathrm{sech}\eta$, where A is an arbitrary constant.

10.8 Finite-difference solution of the Rayleigh equation

To illustrate the implementation of a finite-difference method, we study the stability of an inviscid shear flow in a channel confined between two parallel walls located at $y = -b$ and a, as illustrated in Figure 10.8.1. It is convenient to recast Rayleigh's equation (10.7.23) into the form

$$U(y)\,\frac{\mathrm{d}^2 f}{\mathrm{d}y^2} - \Big(U(y)\,k^2 + \frac{\mathrm{d}^2 U}{\mathrm{d}y^2} \Big) f = c\,\Big(\frac{\mathrm{d}^2 f}{\mathrm{d}y^2} - k^2 f \Big), \tag{10.8.1}$$

where the unknown eigenvalue, c, has been moved to the right-hand side. The no-penetration boundary condition requires that $f(-b) = f(a) = 0$. Because the values of the stream function over the two walls are prescribed to be equal, the disturbance flow will not generate a net flow rate in the direction of the base flow.

10.8.1 Finite-difference equations

We begin by introducing a one-dimensional uniform grid of nodes with N intervals separated by grid spacing $\Delta y = (a + b)/N$, located at y_i for $i = 1, \ldots, N+1$, where $y_1 = -b$ and $y_{N+1} = a$, as illustrated in Figure 10.8.1. For simplicity, we denote the value of f at the

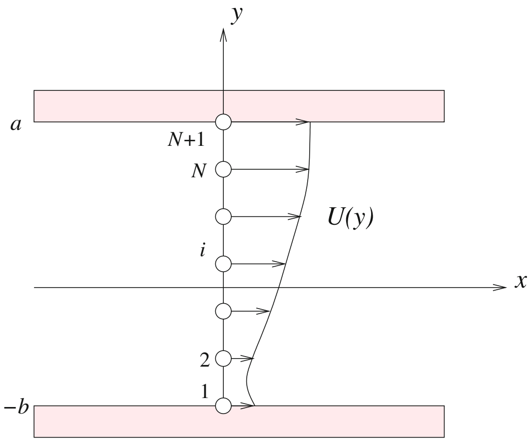

Figure 10.8.1 Illustration of a finite-difference grid used to solve the Rayleigh equation determining the growth rate of two-dimensional perturbations in inviscid unidirectional shear flow.

ith node by $f(y_i) = f_i$. To satisfy the no-penetration condition, we require that the stream function is constant at the lower and upper walls,

$$f_1 = 0, \qquad f_{N+1} = 0. \tag{10.8.2}$$

All other nodal values of f must be computed as part of the solution.

Applying the Rayleigh equation (10.8.1) at the ith interior node for $i = 2, \ldots, N$, and approximating the second derivative, $\mathrm{d}^2 f/\mathrm{d}y^2$, with a centered difference, we obtain the difference equation

$$U_i \, \frac{f_{i+1} - 2\,f_i + f_{i-1}}{\Delta y^2} - (\,U_i\, k^2 + U_i^{''}\,)\, f_i = c\,(\,\frac{f_{i+1} - 2\,f_i + f_{i-1}}{\Delta y^2} - k^2 f_i\,), \tag{10.8.3}$$

where we have denoted $U_i \equiv U(y_i)$ and $U_i^{''} \equiv (\mathrm{d}^2U/\mathrm{d}y^2)(y_i)$. Rearranging, we obtain a difference equation,

$$\begin{aligned} &U_i\, f_{i-1} - \big[\,2\,U_i + \Delta y^2\,(k^2 U_i + U_i^{''}\,)\,\big]\, f_i + U_i\, f_{i+1} \\ &\qquad\qquad = c\,\big[\, f_{i-1} - (2 + k^2 \Delta y^2)\, f_i + f_{i+1}\,\big]. \end{aligned} \tag{10.8.4}$$

Compiling all equations for the interior nodes, $i = 2, \ldots, N$, we derive a system of $N - 1$ linear equations accommodated into the matrix form

$$\mathbf{A} \cdot \mathbf{f} = c\, \mathbf{T} \cdot \mathbf{f}, \tag{10.8.5}$$

where

$$\mathbf{f} \equiv \big[f_2, \quad f_3, \quad \ldots, \quad f_{N-1}, \quad f_N \big] \tag{10.8.6}$$

is the unknown solution vector,

$$\mathbf{A} \equiv \left[\begin{array}{ccc} -2\,U_2 - \Delta y^2(k^2 U_2 + U_2^{''}) & U_2 & 0 \\ U_3 & -2\,U_3 - \Delta y^2(k^2 U_3 + U_3^{''}) & U_3 \\ 0 & U_4 & -2\,U_4 - \Delta y^2(k^2 U_4 + U_4^{''}) \\ \vdots & \vdots & \ddots \\ 0 & 0 & 0 \end{array} \right.$$

$$\longrightarrow \left. \begin{array}{cc} \cdots & 0 \\ \cdots & 0 \\ \cdots & 0 \\ \vdots & \vdots \\ U_N & -2\,U_N - \Delta y^2(k^2 U_N + U_N^{''}) \end{array} \right] \tag{10.8.7}$$

is an $(N-1) \times (N-1)$ tridiagonal matrix involving the nodal velocities of the base flow and its second derivatives, and

$$\mathbf{T} \equiv \begin{bmatrix} -2 - k^2\Delta y^2 & 1 & 0 & \cdots & 0 & 0 \\ 1 & -2 - k^2\Delta y^2 & 1 & \cdots & 0 & 0 \\ 0 & 1 & -2 - k^2\Delta y^2 & \cdots & \cdots & 0 \\ \vdots & \vdots & \ddots & \vdots & \vdots & \vdots \\ 0 & 0 & \cdots & 0 & 1 & -2 - k^2\Delta y^2 \end{bmatrix} \tag{10.8.8}$$

is another $(N-1) \times (N-1)$ tridiagonal matrix. Note that the matrix $\mathbf{T}$ is independent of the velocity profile, $U(y)$.

10.8.2 A generalized eigenvalue problem

Equation (10.8.5) presents us with a generalized algebraic eigenvalue problem that can be stated as follows: Compute a value of the generally complex constant c so that equation (10.8.5) has a nontrivial solution for the vector $\mathbf{f}$, that is, a solution other than the null vector.

To compute an eigenvalue, c, we may restate equation (10.8.5) in the form of a homogeneous equation,

$$\mathbf{E} \cdot \mathbf{f} = \mathbf{0}, \tag{10.8.9}$$

where $\mathbf{E}$ is a tridiagonal matrix given by

$$\mathbf{E} \equiv \begin{bmatrix} E_{1,1} & 1 & 0 & \cdots & 0 \\ 1 & E_{2,2} & 1 & \cdots & 0 \\ \vdots & \vdots & \ddots & \vdots & \vdots \\ 0 & 0 & \cdots & E_{N-2,N-2} & 1 \\ 0 & 0 & \cdots & 1 & E_{N-1,N-1} \end{bmatrix}, \tag{10.8.10}$$

with diagonal elements

$$E_{1,1} = -2 - \Delta y^2 (k^2 + \frac{U_2''}{U_2 - c}), \qquad E_{2,2} = -2 - \Delta y^2 (k^2 + \frac{U_3''}{U_3 - c}),$$
$$\ldots, \qquad E_{N-1,N-1} = -2 - \Delta y^2 (k^2 + \frac{U_N''}{U_N - c}). \tag{10.8.11}$$

Note that the super- and sub-diagonal elements of **E** are all equal to unity.

For system (10.8.9) to have a nontrivial solution, the coefficient matrix **E** must be singular. Phrased differently, c must be such that the determinant of the complex matrix **E** is zero. This observation provides us with a basis for a numerical method involving the following steps:

1. Begin by guessing a complex value for c.
2. Compute the determinant of the matrix **E** using the algorithm discussed in Section 10.8.3.
3. Improve c to reduce the magnitude of the determinant.
4. Return to Step 2 and repeat, if necessary.

The improvement in the third step can be made using Newton's method, setting

$$c^{\text{new}} = c^{\text{old}} - \frac{\det[\mathbf{E}(c^{\text{old}})]}{\left(\frac{\mathrm{d}\det[\mathbf{E}(c)]}{\mathrm{d}c}\right)_{c=c^{\text{old}}}}. \tag{10.8.12}$$

The derivative in the denominator on the right-hand side of (10.8.12) can be approximated with a finite difference,

$$\left(\frac{\mathrm{d}\det[\mathbf{E}(c)]}{\mathrm{d}c}\right)_{c=c^{\text{old}}} \simeq \frac{\det[\mathbf{E}(c^{\text{old}} + \epsilon)] - \det[\mathbf{E}(c^{\text{old}})]}{\epsilon}, \tag{10.8.13}$$

where ϵ is a real or complex increment with small magnitude. Analytic function theory ensures that the derivative is independent of ϵ, provided that the norm of ϵ is small.

10.8.3 Determinant of a tridiagonal matrix

To compute the determinant of the tridiagonal matrix **E**, we use an efficient algorithm that is applicable to a general $M \times M$ tridiagonal matrix of the form

$$\mathbf{T} \equiv \begin{bmatrix} a_1 & b_1 & 0 & \cdots & 0 & 0 & 0 \\ c_2 & a_2 & b_2 & \cdots & 0 & 0 & 0 \\ \vdots & \vdots & \vdots & \ddots & \vdots & \vdots & \vdots \\ 0 & 0 & 0 & \cdots & c_{M-1} & a_{M-1} & b_{M-1} \\ 0 & 0 & 0 & \ldots & 0 & c_M & a_M \end{bmatrix}, \tag{10.8.14}$$

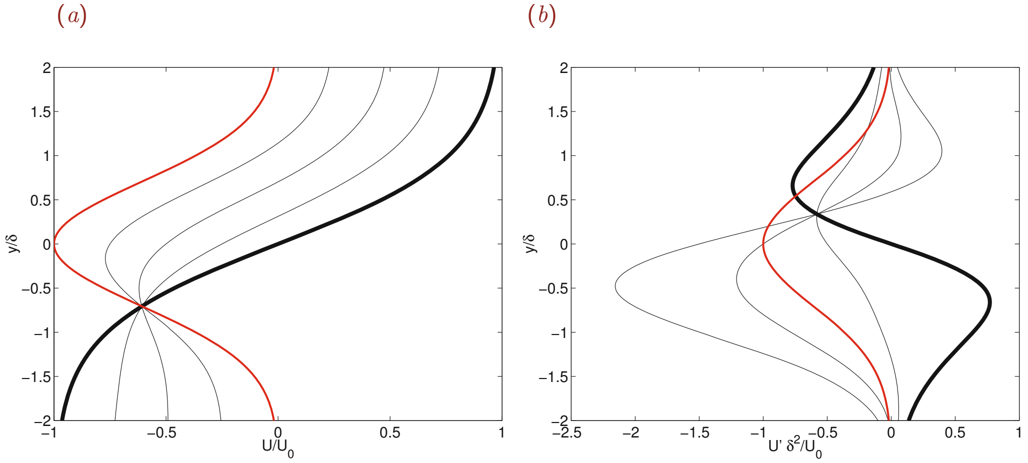

Figure 10.8.2 Profiles of (a) the base flow velocity described by (10.8.16), and (b) its second derivative for $\alpha = 1$ (bold profiles), 0.75, 0.50, 0.25, and 0.

where a_i, b_i, and c_i are real or complex constants. The algorithm involves computing a sequence of numbers, P_i, based on the recursion relations

$$P_1 = a_1, \qquad P_2 = a_2\, a_1 - b_1\, c_2, \qquad \ldots, \qquad P_i = a_i\, P_{i-1} - b_{i-1}\, c_i\, P_{i-2} \tag{10.8.15}$$

for $i = 2, \ldots, M$, and then setting $\det(\mathbf{T}) = P_M$.

10.8.4 Numerical implementation

To be more specific, we consider a family of inviscid shear flows with velocity profile

$$U(y) = U_0\, \big(\, \alpha\, \tanh \eta + (1-\alpha)\, \exp(-\eta^2)\, \big), \tag{10.8.16}$$

where $\eta = y/\delta$, δ is a specified length, and the dimensionless parameter α takes values in the range $[0, 1]$. Profiles of the velocity, $U(y)$, and second derivative, $U''(y)$, are plotted in Figure 10.8.2 for several values of α. The limiting value $\alpha = 1$ corresponds to a shear layer with a hyperbolic tangent velocity profile. The limiting value $\alpha = 0$ corresponds to a symmetric wake with a Gaussian velocity profile.

The following MATLAB function entitled *rayleigh_vel*, located in directory *rayleigh* inside directory *08_stab* of FDLIB, computes the the velocity of the base flow and its first and second derivatives for the flow described by (10.8.16) and another flow with a inverse squared hyperbolic cosine profile:

```
function [U,Up,Upp] = rayleigh_vel (menu,U0,delta,alpha,y)

%-------------------------------------------------------
% Evaluation of the velocity (U), first derivative (Up)
```

```
% and second derivative (Upp), at a point y
%
% menu:  choice of velocity profile
% U0:  coefficient of the velocity profile
% delta:  length scale of the velocity profile
% alpha:  velocity profile parameter
%------------------------------------------------------

%---------
% prepare
%---------

eta = y/delta;

%---------
% evaluate
%---------

%---
if(menu==1)         % derivatives analytically
%---

  alphac = 1.0-alpha; tmp = exp(-eta^2);
  U = alpha*tanh(eta) - alphac*tmp;
  Up = alpha/cosh(eta)^2 + alphac*2.0*eta*tmp;
  Upp = -alpha*2.0*sinh(eta)/cosh(eta)^3 ...
    -alphac*2.0*(1.0-2.0*eta)*tmp;

%---
elseif(menu==2)   % derivatives by numerical differentiation
%---

  U = 1.0/cosh(eta)^2;
  eps = 0.00001;
  U1 = 1.0/cosh(eta-eps)^2;
  U2 = 1.0/cosh(eta+eps)^2;
  Up = (U2-U1)/(2.0*eps);
  Upp = (U2-2.0*U+U1)/eps^2;

%---
else
%---

  disp('rayleigh_vel: this menu item is not available');
  return

%---
end
%---
```

```
%-----
% scale
%-----

Up = Up/delta; Upp = Upp/delta^2;

U = U*U0; Up = Up*U0; Upp = Upp*U0;

%-----
% Done
%-----

return
```

The following MATLAB function entitled *rayleigh_sys*, located in directory *rayleigh* inside directory *08_stab* of FDLIB, compiles the real and imaginary elements of the matrix **E** and computes its determinant:

```
function [detr, deti] = rayleigh_sys (N,Dys,U,Upp,k,creal,cimag)

%---------------------------------
% Compile the (N-1)x(N-1) tridiagonal matrix E
% and compute the determinant
%
% matrix has the structure:
%
%       |a b
%       |  c a b
% E =   |    c a b
%       |      c a b
%
% ar is the real part of a
% ai is the imaginary part of a
%---------------------------------

%---
% generate the complex tridiagonal matrix E
%---

for i=2:N

  den = (U(i)-creal)^2+cimag^2;
  ar(i-1) = -2.0-Dys*(k^2 + Upp(i)*(U(i)-creal)/den);
  br(i-1) = 1.0;
  cr(i-1) = 1.0;

  ai(i-1) = - Dys*Upp(i)*cimag/den;
```

```
  bi(i-1) = 0.0;
  ci(i-1) = 0.0;

end

%---
% Compute the determinant of the complex matrix E
% using a fast method
%---

Pr(1) = ar(1);
Pi(1) = ai(1);
tmpr = br(1)*cr(2)-bi(1)*ci(2);
tmpi = br(1)*ci(2)+bi(1)*cr(2);
Pr(2) = ar(2)*Pr(1)-ai(2)*Pi(1)-tmpr;
Pi(2) = ar(2)*Pi(1)+ai(2)*Pr(1)-tmpi;

for i=3:N-1
  ia = i-1;
  tmpr = br(ia)*cr(i)-bi(ia)*ci(i);
  tmpi = br(ia)*ci(i)+bi(ia)*cr(i);
  ib = i-2;
  auxr = tmpr*Pr(ib)-tmpi*Pi(ib);
  auxi = tmpr*Pi(ib)+tmpi*Pr(ib);
  Pr(i) = ar(i)*Pr(ia)-ai(i)*Pi(ia)-auxr;
  Pi(i) = ar(i)*Pi(ia)+ai(i)*Pr(ia)-auxi;
end

detr = Pr(N-1);
deti = Pi(N-1);

%-----
% done
%-----

return
```

The following MATLAB code entitled *rayleigh,* located inside directory *08_stab* of FDLIB, computes the complex phase velocity of perturbations and generates a stability graph:

```
%------------------------------------------------
% Normal mode analysis of unidirectional inviscid
% shear flow along the x axis
%
% The flow is confined between two parallel walls
% located at y = a and -b
%
% SYMBOLS:
% -------
```

```
%
% U: velocity, function of y
% Upp:  second derivative of U with respect to y
% N: level of discretization of y axis within (a,b)
%
% kdiv:  number of k divisions
%         will span the wave-number range (kmin, kmax)
%
% epsr:  real step for Newton corrections
% epsi:  imag step for Newton corrections
% tole:  tolerance for convergence
%
% cr, ci:  real and imaginary parts of c
%---------------------------------------------

a = 5.0;
b = 5.0;
menu = 1;
U0 = 1.0;
delta = 1.0;
alpha = 1.0;

N = 2*2*64;

kstart = 0.01;
kend = 2.0;
kdiv = 64;
newter = 20;   % max Newton iterations
epsr = 0.01;   % for Newton iterations
epsi = 0.01;   % for Newton iterations
tole = 0.000001;   % for stopping Newton iterations

cr = 0.7;   % initial guess
ci = 0.1;   % initial guess

%--------
% prepare
%--------

denn = epsr^2 + epsi^2;
Dk = (kend-kstart)/kdiv;

Dy = (a+b)/N;
Dys = Dy^2;

%----------
% velocity profile
%----------
```

```
for i=1:N+1

  y = -b+(i-1)*Dy;

  [U(i),Up(i),Upp(i)] = rayleigh_vel(menu,U0,delta,alpha,y);

end

%---------------------------------------------------
% scan the wave-number axis from k = kstart to kend
%---------------------------------------------------

%=======================
for kloop=1:kdiv+1
%=======================

k = kstart+(kloop-1)*Dk;


%---
% Newton iterations
%---

  %---
  for iter=1:newter
  %---

    [detr, deti] = rayleigh_sys (N,Dys,U,Upp,k,cr,ci);

    [detr1, deti1] = rayleigh_sys (N,Dys,U,Upp,k,cr+epsr,ci+epsi);

%---
% compute the derivative DdetDc = d(det(E))/dc
%---

    Ddetr = detr1-detr;
    Ddeti = deti1-deti;

    DdetDcr = ( Ddetr*epsr + Ddeti*epsi)/denn;
    DdetDci = (-Ddetr*epsi + Ddeti*epsr)/denn;

%---
% compute the correction
%---

    den = DdetDcr^2+DdetDci^2;
    corrr = ( detr*DdetDcr + deti*DdetDci)/den;
    corri = (-detr*DdetDci + deti*DdetDcr)/den;
```

```
%---
% make the correction
%---

    cr = cr - corrr;
    ci = ci - corri;

    corr = sqrt(corrr^2+corri^2);

    if(corr<tole)
      break
    end

%---
  end   % of Newton iterations
%---

%---
% printing session
%---

sigma = ci*k;

kplot(kloop) = k;
crplot(kloop) = cr;
ciplot(kloop) = ci;
sigmaplot(kloop) = sigma;

if(ci<0.001)
  break
end

%===
end   % of scanning the wave number
%===

figure(1)
plot(kplot,ciplot,'k-','linewidth',1)

figure(2)
plot(kplot,sigmaplot,'k-','linewidth',1)

figure(3)
plot(kplot,crplot,'k-','linewidth',1)
```

Note that, because the code does not make use of internal MATLAB functions, it can be translated into any mid-level computer language of choice; this is a poor man's code.

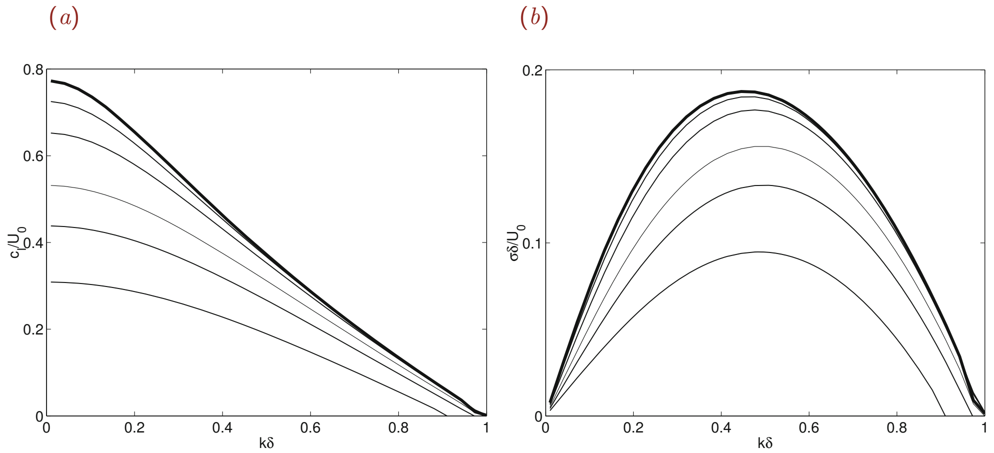

Figure 10.8.3 Instability of an inviscid shear flow with hyperbolic tangent velocity profile described by equation (10.8.16) with $\alpha = 1$. Graphs of (a) the scaled imaginary part of the phase velocity, $c_{\rm I}/U_0$, and (b) scaled growth rate, $\sigma_{\rm I}\delta/U_0$, for $a/\delta = b/\delta = 2.0,\ 2.5,\ 3.0,\ 4.0,\ 5.0$, and 6.0 (heavy lines), in the regime of unstable wave numbers.

Results of numerical computations for an inviscid shear flow with hyperbolic tangent velocity profile described by equation (10.8.16) with $\alpha = 1$ are shown in Figure 10.8.3 for a sequence of channel widths, a/δ, with $b = a$. When the scaled wave number, $k\delta$, is higher than a critical threshold, $(k\delta)_{\rm cr}$, that is determined by the ratio a/δ, the growth rate is zero and the perturbations are neutrally stable. As a/δ tends to infinity, we obtain infinite shear flow in the absence of side walls. In this limit, the critical wave number for neutral stability is known to be exactly $(kb)_{\rm cr} = 1.0$.

The results shown in Figure 10.8.3 demonstrate that the walls diminish the growth rate of perturbations by restricting the lateral extent over which fluid motion is allowed to develop. Maximum growth rate occurs at a certain wave number $(kb)_{\rm max} \simeq 0.50$. The corresponding perturbation is expected to dominate the instability and therefore spontaneously arise in a randomly perturbed flow.

PROBLEM

10.8.1 *Instability of inviscid shear flow*

(a) Run the code *rayleigh* to generate the counterpart of Figure 10.8.3 for the velocity profile given in (10.8.16) with $\alpha = 0.50$ and 0.0, in each case for $b = a$ and $a/\delta = 2.0$, 3.0, and 4.0. Discuss the results of your computations.

(b) Repeat (a) for a shear flow with velocity profile

$$U(y) = U_0\left(\alpha\,\tanh\eta + (1-\alpha)\,{\rm sech}^2\eta\right), \qquad (10.8.17)$$

where $\eta = y/\delta$, δ is a specified length, and the dimensionless parameter α takes values in the range $[0, 1]$. The limiting values $\delta = 1$ and 0 correspond, respectively, to a shear layer with a hyperbolic tangent velocity profile and to the Bickley jet.

10.9 Finite-difference solution of the Orr–Sommerfeld equation

Finite-difference methods for the Orr–Sommerfeld equation (10.7.22) governing the stability of viscous unidirectional flow can be developed working as in Section 10.8 for the Rayleigh equation governing the stability of inviscid flow. To begin, we rearrange the Orr–Sommerfeld equation by moving the complex phase velocity, c, to the right-hand side, obtaining

$$\begin{aligned} \mathrm{i}\nu\, k\,\Big(-2\,\frac{\mathrm{d}^2 f}{\mathrm{d}y^2} + k^2 f\Big) + \mathrm{i}\,\frac{\nu}{k}\,\frac{\mathrm{d}^4 f}{\mathrm{d}y^4} + U(y)\,\Big(\frac{\mathrm{d}^2 f}{\mathrm{d}y^2} - k^2 f\Big) - \frac{\mathrm{d}^2 U}{\mathrm{d}y^2}\, f \\ = c\,\Big(\frac{\mathrm{d}^2 f}{\mathrm{d}y^2} - k^2 f\Big). \end{aligned} \qquad (10.9.1)$$

The no-penetration and no-slip boundary conditions over a stationary solid surface require that the boundary values of the function $f(y)$ and its first derivative are both zero.

Finite-difference equations

Discretizing the Orr–Sommerfeld equation, as discussed in Section 10.8, we obtain a system of linear equations,

$$\mathbf{A}\cdot\mathbf{f} = c\,\mathbf{B}\cdot\mathbf{f}, \qquad (10.9.2)$$

where $\mathbf{B}$ is a tridiagonal matrix. However, because of the presence of the fourth derivative, $f^{(iv)}$, the matrix $\mathbf{A}$ is pentadiagonal (*penta* derives from the Greek word $\pi\epsilon\nu\tau\epsilon$ which means five.) The algebraic system arising from the finite-difference discretization can be recast into a form similar to that shown in (10.8.9),

$$\mathbf{E}\cdot\mathbf{f} = \mathbf{0}, \qquad (10.9.3)$$

where the matrix $\mathbf{E}$ is now pentadiagonal. Unfortunately, the determinant of this matrix may no longer be computed using an efficient numerical method.

As a compromise, we reluctantly solve the generalized eigenvalue problem expressed by (10.9.2) using an internal MATLAB function regarded as a black box. The pertinent MATLAB function call is:

```
egv = eig(A,B)
```

where the output vector `egv` contains the eigenvalues. Our simple task is to compile the matrices $\mathbf{A}$ and $\mathbf{B}$ provided in the input.

Finite-difference equations

Consider the finite-difference grid shown in Figure 10.8.1. To derive the difference equation corresponding to the ith interior node, we use a familiar finite-difference approximation for the second derivative,

$$f_i'' = \frac{f_{i-1} - 2f_i + f_{i+1}}{\Delta y^2} \tag{10.9.4}$$

for $i = 2, \ldots, N$, subject to the no-penetration boundary condition requiring that $f_1 = 0$ and $f_{N+1} = 0$. The corresponding approximation for the fourth derivative is

$$f_i^{(iv)} = \frac{f_{i-2} - 4f_{i-1} + 6f_i - 4f_{i+1} + f_{i+2}}{\Delta y^4} \tag{10.9.5}$$

for $i = 2, \ldots, N$, subject to the no-penetration boundary condition requiring that $f_1 = 0$ and $f_{N+1} = 0$ and to the no-slip boundary condition requiring that $f_0 = f_2$ and $f_{N+2} = f_N$.

Orr–Sommerfeld code

By way of example, we consider an infinite shear flow with a hyperbolic tangent velocity profile

$$U(y) = U_0 \tanh \eta, \tag{10.9.6}$$

where $\eta = y/\delta$ and δ is a specified length, and a pressure-driven channel flow with a parabolic velocity profile

$$U(y) = U_0\,(1 - \eta^2), \tag{10.9.7}$$

where $\eta = y/a$ and $y = \pm a$ describes the location of the walls.

The following MATLAB code entitled *orr*, located in directory *08_stab* of FDLIB, implements the numerical method and generates stability graphs by running over the wave number and the Reynolds number in two nested loops:

```
%====================
% Solution of the Orr--Sommerfeld equation
% in a domain -b<y<a
%
% N finite-difference divisions
%
% ====+ N+1 y=a
% |
% + N
% |
% +
% |
% + 2
% |
% ====+ 1 y=-b
%
% iflow = 1 hyperbolic tangent profile
% iflow = 2 parabolic Hagen-Poiseuille flow
```

```
%
% U0:  reference velocity
%====================

%---
% preferences
%---

iflow = 2;   % parabolic Hagen--Poiseuille flow
iflow = 1;   % hyperbolic tangent profile

kmax = 1.2;   % maximum wave number
nkloop = 32;   % number of wave numbers
N = 256;   % discretization level

%---
% plotting flags
%---

iplot2d = 1;
iplotcn = 1;
iplotms = 1;

%---
% choose the flow and set parameters
%---

if(iflow==1)
  a = 5.0;
  b = 5.0;
  U0 = 1.0;
  delta = 1.0;
  Restart = 1.0;   % starting Reynolds number
  Reend = 40.0;   % ending Reynolds number
  nReloop = 16;   % number of Re scanned
elseif(iflow==2)
  a = 1.0;
  b = a;
  U0 = 1.0;
  Restart = 2000.0;
  Reend = 40000.0;
  nReloop = 32;
end

%---
% prepare
%---

Dy = (a+b)/N;   % grid size
```

```
Dys = Dy^2;
Dk = kmax/nkloop;
im = sqrt(-1);   % imaginary unit
  % factor for ramping Re
fcRe = (Reend/Restart)^(1/(nReloop-1));

%---
% nodal velocity and second derivatives
%---

for i=1:N+1

  y(i) = -b+(i-1.0)*Dy;

  if(iflow==1)
    eta = y(i)/delta;
    U(i) = U0*tanh(eta);
    Upp(i) = -2.0*U0*sinh(eta)/cosh(eta)^3;
  elseif(iflow==2)
    eta = y(i)/a;
    U(i) = U0*(1.0-eta^2);
    Upp(i) = -2.0*U0;   % second derivative
  end

end

%------------------------------------
% pentadiagonal matrix approximating
% the fourth derivative f''''
%------------------------------------

P = zeros(N-1,N-1);

P(1,1)= 7.0; P(1,2)=-4.0; P(1,3)= 1.0;
P(2,1)=-4.0; P(2,2)= 6.0; P(2,3)=-4.0; P(2,4)= 1.0;

for i=3:N-3
  P(i,i-2)=1; P(i,i-1)=-4; P(i,i)=6; P(i,i+1)=-4; P(i,i+2)=1;
end

P(N-2,N-4)= 1.0; P(N-2,N-3)=-4.0; P(N-2,N-2)= 6.0;
    P(N-2,N-1)=-4.0;
        P(N-1,N-3)= 1.0; P(N-1,N-2)=-4.0; P(N-1,N-1)= 7.0;
P = P/Dy^4;

%------------------------------------
% tridiagonal matrix approximating
% the second derivative f''
%------------------------------------
```

```
T = zeros(N-1,N-1);

T(1,1) = -2.0; T(1,2) =1.0;

for i=2:N-2
  T(i,i-1)=1.0; T(i,i)=-2.0; T(i,i+1)=1.0;
end

T(N-1,N-2) = 1.0; T(N-1,N-1) =-2.0;

T = T/Dys;

%---------------------------
% another tridiagonal matrix
% approximating U f''
%---------------------------

T1 = zeros(N-1,N-1);

T1(1,1) = -2.0*U(2); T1(1,2) = U(2);

for i=2:N-2
  Unode = U(i+1);
  T1(i,i-1) = Unode; T1(i,i) = -2.0*Unode; T1(i,i+1) = Unode;
end

T1(N-1,N-2) = U(N); T1(N-1,N-1) = -2.0*U(N);

T1 = T1/Dys;

%==================
% scan the wave number (k)
%==================

%---
for kloop=1:nkloop+1
%---

k = (kloop-1.0)*Dk+0.0001;

ks = k*k;

%==================
% scan the Reynolds number
%==================

  Re = Restart;
```

```
%---
for Reloop=1:nReloop
%---

  if(iflow==1)         % adjust the kinematic viscosity
    nu = U0*delta/Re;   % according to Re
  elseif(iflow==2)
    nu = U0*a/Re;
  end

  A = im*nu/k * P + T1- 2.0*k*im*nu*T;

  for i=1:N-1
    A(i,i) = A(i,i) - U(i+1)*ks - Upp(i+1) + im*nu*k^3;
  end

  B = T;
  for i=1:N-1
    B(i,i) = B(i,i)-ks;
  end

%---
% eigenvalues
%---

  egv = eig(A,B);

  gr = imag(k*egv);   % growth rate
  grsorted = -sort(-gr);   % sort the growth rate
  ggrr(kloop,Reloop) = grsorted(1);   % maximum growth rate

  if(iflow==1)
    wn(kloop) = k*delta;
  elseif(iflow==2)
    wn(kloop) = k*a;
  end

  Re = fcRe*Re;   % ramp up Re

%---
end   % of Reloop
%---

Re = Re/fcRe;

%---
end   % of kloop
%---
```

```
%=======
% Graphics module
%=======

%--------
% 2D plot
%--------

if(iplot2d==1)

  figure(1)
  hold on
  set(gca,'fontsize',15)
  box on

  if(iflow==1)
    xlabel('k\delta','fontsize',15)
    ylabel('\sigma_I\delta/U_0','fontsize',15)
    axis([0 1.2 -0.2 0.2])
  elseif(iflow==2)
    xlabel(’ka’,’fontsize’,15)
    ylabel('\sigma_I{a}/U_0','fontsize',15)
    axis([0 1.2 -0.06 0.01])
  end

  plot(wn,ggrr(:,1),'k','linewidth',3);

  for Reloop=2:nReloop
    plot(wn,ggrr(:,Reloop),'k');
  end

  plot([0 1.2],[0,0],'--k')

end

%----
% contour plot
%----

if(iplotcn==1)

  figure(2)
  hold on
  set(gca,’fontsize’,15)
  box on
  xlabel(’Re’,’fontsize’,15)

  if(iflow==1)
    [C,h] = contour(Rey,wn,ggrr,[0.0, 0.0],'k-');
```

```
    set(h, 'LineWidth', 3);
    clabel(C,h);
    [C,h]= contour(Rey,wn,ggrr,[-0.2, -0.2],'k');
    clabel(C,h);
    [C,h]= contour(Rey,wn,ggrr,[-0.1, -0.1],'k');
    clabel(C,h);
    [C,h]=contour(Rey,wn,ggrr,[0.05, 0.05],'k');
    clabel(C,h);
    [C,h]=contour(Rey,wn,ggrr,[0.10, 0.10],'k');
    clabel(C,h);
    [C,h]=contour(Rey,wn,ggrr,[0.14, 0.14],'k');
    clabel(C,h);
    ylabel('k\delta','fontsize',15)
    axis([0 40 0 1])
  elseif(iflow==2)
    [C,h]=contour(Rey,wn,ggrr,[0.0, 0.0],'k-');
    plot([5572 5572],[0.55,1.2],'k--')
    ylabel('ka','fontsize',15)
    axis([0 40000 0.55 1.2])
  end

end

%----
% mesh plot
%----

if(iplotms==1)

  figure(3)

  set(gca,'fontsize',15)
  mesh(Rey,wn,ggrr);
  box on
  xlabel('Re','fontsize',15)

  if(iflow==1)
    zlabel('\sigma_I\delta/U_0','fontsize',15)
    ylabel('k\delta','fontsize',15)
    axis([0 40 0 1 -1.5 0.2])
  elseif(iflow==2)
    zlabel('\sigma_I{a}/U_0','fontsize',15)
    ylabel('ka','fontsize',15)
    axis([0 40000 0 1.2 -0.06 0.01])
  end

end
```

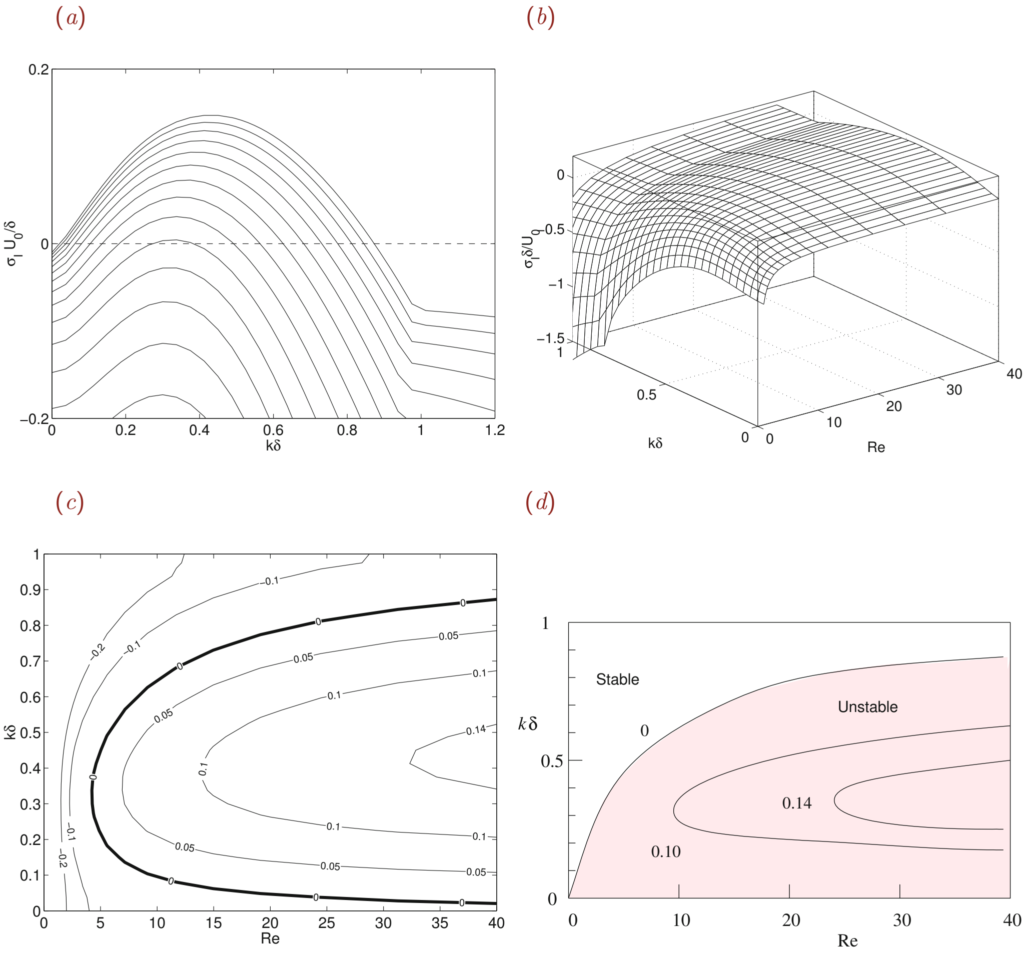

Figure 10.9.1 Stability graphs for infinite shear flow with velocity profile $U(y) = U_0 \tanh\eta$, where $\eta = y/\delta$ and δ is a specified length. (a) Scaled growth rate, $\sigma_I\delta/U_0$, computed with discretization level $N = 256$ and truncation level $a = b = 5\delta$, plotted against the scaled wave number, $k\delta$, for Reynolds number $\mathrm{Re} \equiv U_0\delta/\nu = 1$ (lowest curve) up to 40 (highest curve), increasing by a geometrical factor. (b) Scaled growth rate plotted against $k\delta$ and Re, and (c) displayed as a contour plot. (d) Schematic illustration of the countour plot of the scaled growth rate in the absence of numerical error, showing regimes of stable and unstable flow.

Infinite shear flow

Results of numerical computations for infinite shear flow with $N = 256$ divisions and domain trunction level $a = b = 5\,\delta$ are shown in Figure 10.9.1$(a$–$c)$. The zeroth contour in Figure 10.9.1(c), indicated by the bold line, corresponds to neutrally stable perturbations.

A schematic yet faithful contour plot of the growth rate for flow in an infinite domain, $a, b \to \infty$, is shown in Figure 10.9.1(d). A perturbation whose wave number lies in the shaded area below the zeroth-level contour is unstable, whereas a perturbation whose wave number lies above the shaded area is stable. As the Reynolds number increases, we recover the results for inviscid flow presented in Figure 10.8.3.

The results in Figure 10.9.1(d) reveal that the flow is unstable at arbitrarily small Reynolds numbers. The destabilizing effect of inertia becomes evident by observing that, as the Reynolds number increases, the range of unstable scaled wave numbers, $[0, (k\delta)_{\rm cr}]$, becomes wider, which means that a broader range of perturbations grow at increasingly high growth rates.

Plane Hagen–Poiseuille flow

Results of numerical computations with $N = 128$ divisions for plane Hagen–Poiseuille (pressure-driven) flow in a channel confined between two parallel walls located at $y = \pm a$ are shown in Figure 10.9.2. The zeroth contour of the growth rate displayed in Figure 10.9.2 (c) separates regions of stable flow (outside the loop) and unstable flow (inside the loop). The Reynolds number for instability, $\text{Re}_{\rm cr} = 5,772$, represented by the vertical dashed line in Figure 10.9.2 (c), defines the critical threshold where certain wave numbers, and thus the flow itself, start becoming unstable.

PROBLEMS

10.9.1 *Stability of a generalized shear flow*

Derive the finite-difference formula (10.9.5) from (10.9.4).

10.9.2 💻 *Stability of a generalized shear flow*

Generate and discuss the counterpart of Figure 10.9.1 for the velocity profile given in (10.8.16) with $\alpha = 0.5$ or 0.0.

10.10 Turbulent flow

Turbulent flow is established when the Reynolds number, defined in an appropriate fashion for the particular flow under consideration, $\text{Re} = \rho V L/\mu$, exceeds a certain threshold, usually on the order of 10^3.

In the definition of the Reynolds number, V is a characteristic macroscopic velocity and L is a characteristic macroscopic length typically associated with the size of the boundaries. Both V and L are classified as *external scales*. For example, in the case of pipe flow, V can be identified either with the mean fluid velocity or with the maximum fluid velocity occurring at the centerline, and L can be identified with the tube radius or diameter.

Turbulence is characterized by random motions in *both* time and space. Thus, a graph of a velocity component plotted against time at a particular location in a turbulent flow

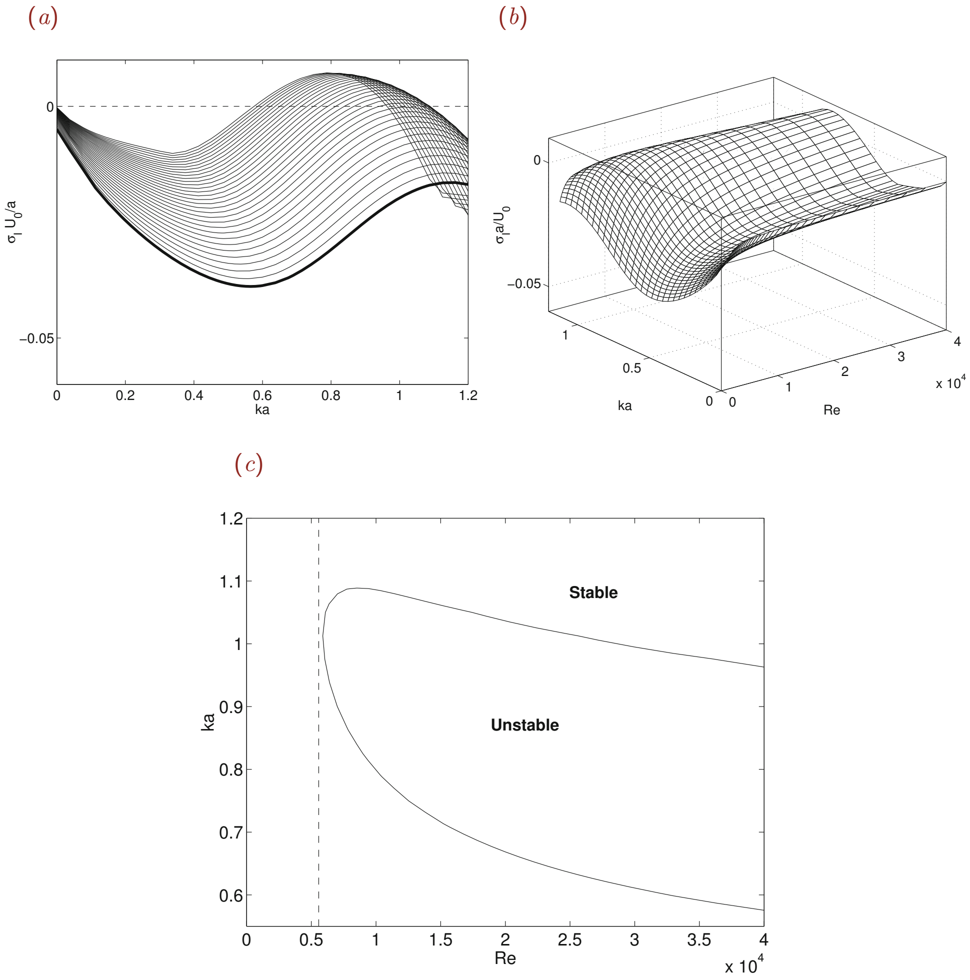

Figure 10.9.2 Stability graphs for unidirectional plane Hagen-Poiseuille flow in a channel confined between two parallel walls located at $y = \pm a$, with velocity profile $U(y) = U_0\,(1 - y^2/a^2)$, where U_0 is the midplane velocity. (a) Scaled growth rate, $\sigma_I a/U_0$, plotted against the scaled wave number, ka, for Reylonds numbers $\mathrm{Re} \equiv U_0 a/\nu = 2,000$ (lowest curve printed in bold) up to $40,000$, increasing by a geometrical factor. (b) Scaled growth rate plotted against ka and Re. (c) Zero contour of the growth rate separating regions of stable flow (outside the loop) and unstable flow (inside the loop).

reveals random fluctuations, as illustrated in Figure 10.10.1(a). An analogous graph of the velocity against the spatial coordinate x at a particular instant in time reveals similar random fluctuations, as illustrated in Figure 10.10.1(b).

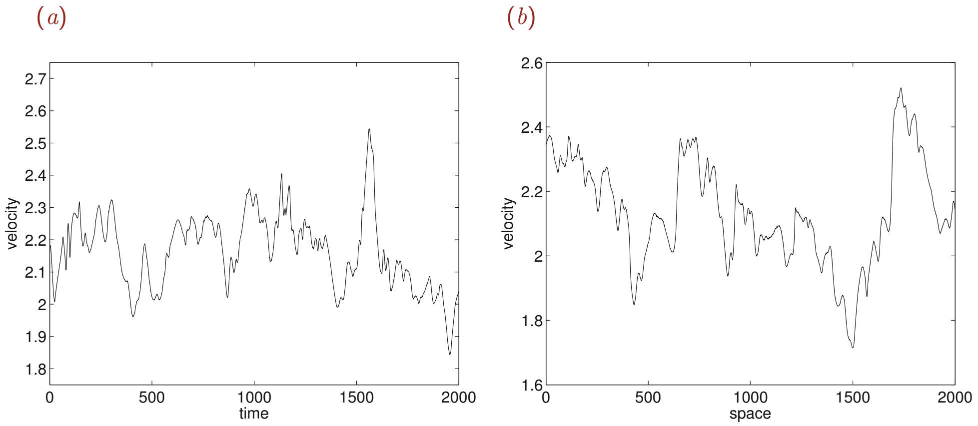

Figure 10.10.1 Typical (a) temporal and (b) spatial variation of a velocity component in a turbulent flow.

10.10.1 Transition to turbulence

The transition from laminar to turbulent flow with increasing Reynolds number is not sudden, but occurs through a sequence of events that lead to an eventual randomly fluctuating motion. For example, pressure-driven flow in a circular tube is laminar when the Reynolds number, defined with respect to the tube radius and the maximum velocity at the centerline, is less than approximately $1,100$; transition occurs when the Reynolds number lies between $1,100$ and $1,500$; and fully developed turbulent motion is established at higher Reynolds numbers. Wall roughness and entrance conditions affect the precise thresholds for transition.

A record of the streamwise velocity component in uniform (streaming) flow past a flat plate with length L at a sequence of increasing Reynolds numbers, defined with respect to the length of the plate, is shown in Figure 10.10.2.[3] In the experiment, the velocity probe was placed $0.02''$ above the plate and $56''$ in behind the leading edge, where the double prime stands for an inch. The graphs illustrate the onset of oscillations, the development of turbulent spots, and the ultimate establishment of fully turbulent flow.

Logistic mapping

A simple model illustrating the process of transition from simple to complex behavior is provided by the logistic mapping. Given a number, $x^{(0)}$, the logistic mapping generates a sequence of numbers, $x^{(1)}, x^{(2)}, \ldots$, computed by the recursion formula

$$x^{(k+1)} = \lambda\, x^{(k)}\,(1 - x^{(k)}) \tag{10.10.1}$$

for $k = 0, 1, \ldots$, where λ is a specified positive constant. The special choices $x^{(0)} = 0$ and $(\lambda - 1)/\lambda$ are the fixed points of the mapping; for these choices, $x^{(k)} = x^{(0)}$ for all k, and the logistic sequence is stationary.

---

[3] Cebeci, T. & Smith, A. M. O. (1974) *Analysis of Turbulent Boundary Layers*, Academic Press.

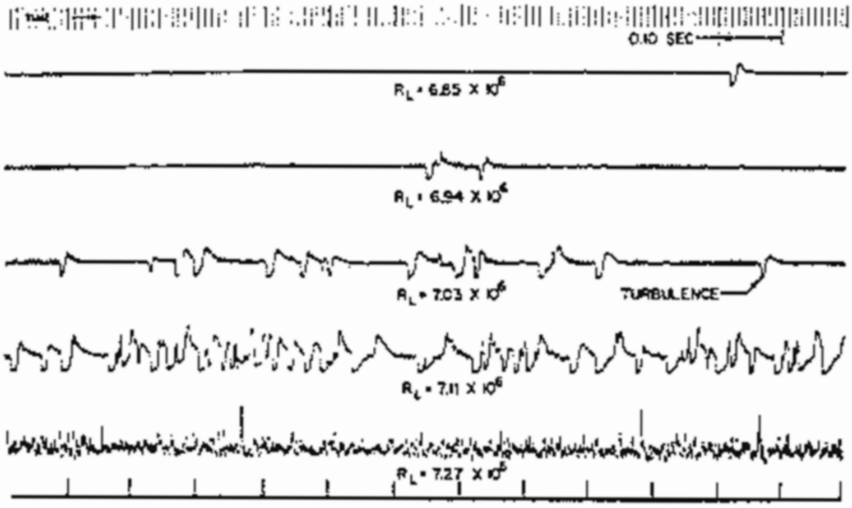

Figure 10.10.2 Record of the streamwise velocity component in flow past a flat plate at a sequence of increasing Reynolds numbers, Re_L, defined with respect to the length of the plate, L. The signal shows the onset of oscillations, the development of turbulent spots, and the ultimate establishment of fully turbulent flow.

To illustrate the transition, we introduce the λx plane and perform a series of computations according to the following steps:

1. Choose a value for λ.
2. Select a value for $x^{(0)}$ that lies between 0 and 1, but is not exactly equal to 0 or 1.
3. Compute a few hundred terms based on the logistic mapping (10.10.1).
4. Skip the first one hundred terms and plot the rest of the terms in the λx plane with dots.
5. Return to Step 1 and repeat.

The results of this computation are shown in Figure 10.10.3. We observe that, as the parameter λ increases, a cascade of bifurcations and a random behavior reminiscent of turbulent motion emerges.

10.10.2 Lagrangian turbulence

Point particles in a certain class of unsteady two-dimensional laminar flows and steady or unsteady three-dimensional laminar flows have been observed to move in a random fashion,

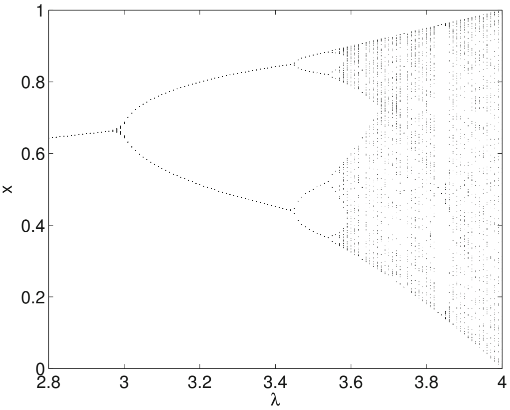

Figure 10.10.3 Sequences generated by the logistic mapping equation (10.10.1), illustrating the process of transition by way of a cascade of bifurcations in the λx plane.

exhibiting a Lagrangian turbulent motion. However, fluid motion in a turbulent flow should be distinguished from the seemingly random motion of point particles in these laminar yet chaotic flows. A distinguishing feature of a turbulent flow is the presence of pronouced three-dimensional vorticity fluctuations and the occurrence of significant kinematic and molecular diffusion accompanied by high levels of viscous dissipation.

10.10.3 Features of turbulent motion

Turbulence continues to defy a simple physical interpretation in terms of elementary fluid motions. In a traditional approach, a turbulent flow is regarded as a stochastic random process amenable to statistical analysis. However, several important features distinguish turbulent motion from a generic random process.

Intermittency

Turbulence is intermittent. A record of the velocity at a certain point in a turbulent flow may appear regular for a period of time, only to be interrupted by periods of violent turbulent motion in an intermittent fashion.

Coherent structures

A turbulent flow contains small-scale short-lived and large-scale long-lived coherent structures associated with eddies and vortices with a well-defined structure. Examples include vortex billows developing in shear layers and horseshoe vortices developing near boundary layers and in regions of high shear rates.

Vortex motion

An intimate connection exists between the dynamics of a turbulent flow and vortex dynamics discussed in Chapter 11. However, it is not clear how studies of vortex dynamics can be used to delineate precisely the physical and mathematical properties of a turbulent flow.

Eddy motion

Eddies in a turbulent flow carry turbulent kinetic energy that is distributed over a broad range of scales; from the external scale, L, to the energy dissipating Kolmogorov scale, η, defined later in Section 10.10.6. Energy is transferred across the scales, forward and backward, from large to small and small to large, and a balance is achieved at dynamic equilibrium. A net transfer of energy occurs toward the small scales.

Dependence on the type of flow

The dynamics of turbulent flow associated with eddy motion and the distribution of energy among the different length scales is not universal, but depends on the particular flow under consideration. Thus, the properties of wall-bounded turbulent shear flow are different from those of unbounded shear flow, and different from those of grid-turbulent flow generated behind a grid placed in a high-speed flow. This diversity reflects differences in the physical mechanism by which energy is supplied into a turbulent flow, ultimately to be dissipated by small-scale motion.

Sedation near a wall

The no-slip boundary condition sedates the turbulent motion near a wall where a viscous sublayer of an unsteady laminar flow is established. A buffer zone separates the viscous sublayer from the regime of fully-developed turbulent flow. The temporal velocity signal of a turbulent flow inside a circular pipe of radius 15 cm is shown in Figure 10.10.4 at different radial positions. The measurements illustrate the cessation of the turbulent motion near the wall.

10.10.4 Decomposition into mean and fluctuating components

It is useful to decompose a turbulent flow variable, such as a velocity component, into a smoothly varying or mean component and a rapidly fluctuating component. The smoothly varying component can be identified with the time averaged value over a period of time, t_0, that is large compared to the time scale of the fluctuations, but small compared to the external time scale L/V.

The mean velocity at the position $\mathbf{x}$, designated by an overbar, is defined as

$$\overline{\mathbf{u}}(\mathbf{x}, t) \equiv \frac{1}{t_0} \int_{t-\frac{1}{2}t_0}^{t+\frac{1}{2}t_0} \mathbf{u}(\mathbf{x}, t+t')\, \mathrm{d}t'. \tag{10.10.2}$$

The fluctuating velocity, designated by a prime, is then defined by the decomposition

$$\mathbf{u}(\mathbf{x}, t) = \overline{\mathbf{u}}(\mathbf{x}, t) + \mathbf{u}'(\mathbf{x}, t). \tag{10.10.3}$$

Note that the mean component is allowed to be a slowly varying function of time. The fluctuating component evolves rapidly in time.

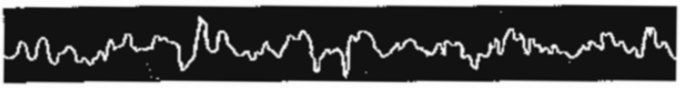

(a) $r = 0$ (on axis)

(b) $r = 4.5$ cm

(c) $r = 7.5$ cm

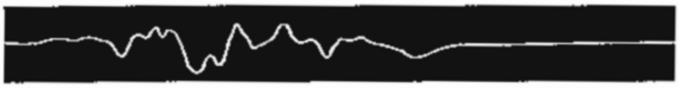

(d) $r = 9.5$ cm

(e) $r = 14.5$ cm

Figure 10.10.4 Temporal velocity fluctuations in turbulent pipe flow at different distances from the tube wall, showing the presence of the laminar sublayer and the buffer zone near the wall, after Corrsin, S. (1943) Investigation of flow in an axially asymmetric heated jet-air. *NACA Rep. 3L23*.

The definition (10.10.2) implies that the time-averaged value of the fluctuating velocity is zero by construction,

$$\overline{\mathbf{u}'}(\mathbf{x}, t) \equiv \frac{1}{t_0} \int_{t-\frac{1}{2}t_0}^{t+\frac{1}{2}t_0} \mathbf{u}'(\mathbf{x}, t + t')\,\mathrm{d}t' = \mathbf{0}. \tag{10.10.4}$$

In contrast, the time averaged value of the square of the x component of the fluctuating velocity,

$$\overline{u_x'^2}(\mathbf{x}, t) \equiv \frac{1}{t_0} \int_{t-\frac{1}{2}t_0}^{t+\frac{1}{2}t_0} u_x'^2(\mathbf{x}, t + t')\,\mathrm{d}t', \tag{10.10.5}$$

is not zero; the square of the y or z component of the fluctuating velocity is also nonzero. The square root of these time averages, called the root-mean-square (rms) values, normalized by an external velocity scale, V, expressed by the ratios

$$i_x \equiv \frac{1}{V}\sqrt{\overline{u_x'^2}}, \qquad i_y \equiv \frac{1}{V}\sqrt{\overline{u_y'^2}}, \qquad i_z \equiv \frac{1}{V}\sqrt{\overline{u_z'^2}}, \tag{10.10.6}$$

are sensible measures of the intensity of the turbulent motion in the three spatial directions.

Laboratory measurements have shown that the three intensities defined in (10.10.6) have different magnitudes, except in the idealized case of isotropic turbulent flow occurring in the absence of boundaries. Nearly isotropic turbulence can be realized in the laboratory by placing eight fans at the vertices of a cube, and turning the rotating blades of the fans toward the center of the cube. In the case of channel or tube flow, the turbulence intensity in the direction of the flow is significantly greater than that in directions perpendicular to the flow, especially near walls.

A single measure of the magnitude of the turbulent velocity fluctuations is provided by the velocity scale

$$u \equiv \Big(\frac{\overline{u_x'^2} + \overline{u_y'^2} + \overline{u_x'^2}}{3} \Big)^{1/2}. \tag{10.10.7}$$

In the case of isotropic turbulence, the three terms in the numerator on the right-hand side are equal.

Flow through a pipe

As an example, we consider pressure-driven turbulent flow through a circular tube of radius a. Schematic illustrations of the mean velocity profile, distribution of the streamwise turbulence intensity, and distribution of the lateral turbulence intensity are shown in Figure 10.10.5. The mean velocity profile can be approximated with the algebraic form

$$\overline{u}_x(\sigma) = U \left(1 - \frac{\sigma}{a}\right)^{1/7}, \tag{10.10.8}$$

where $U \equiv (\overline{u}_x)_{max}$ is the maximum mean velocity occurring at the centerline. This profile should be contrasted with its parabolic counterpart for laminar flow shown in equation (7.3.8).

10.10.5 Inviscid scales

A turbulent flow contains an infinite collection of interacting eddies defined and regarded as elementary fluid motions. Inspecting the turbulence signal shown in Figure 10.10.1(b), we identify spatial scales with a broad range of magnitudes. One important scale, classified as inviscid, is the scale of the energy-containing turbulent motion, denoted by ℓ.

Using ℓ and the magnitude of the velocity fluctuations u defined in (10.10.7), we deduce that the time scale of the energy containing eddies is comparable to ℓ/u. The actual size of ℓ varies according to the particular flow under consideration, as follows:

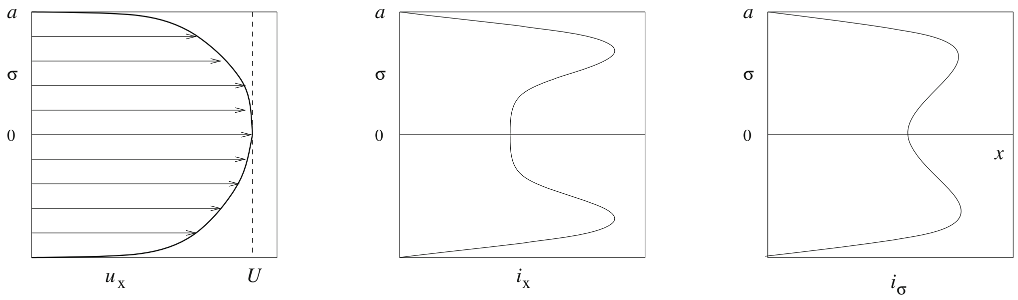

Figure 10.10.5 Schematic illustrations of the mean velocity profile and distribution of the streamwise and lateral turbulence intensities for turbulent flow through a circular tube of radius a.

- In the case of boundary-layer flow, ℓ is comparable to the local boundary layer thickness.
- In the case of turbulent jet flow, ℓ is comparable to the local jet diameter.
- In the case of a wake behind a body, ℓ is comparable to the local width of the wake.
- In the case of pipe flow, ℓ is comparable to the tube diameter.
- In the case of infinite shear flow over a wall, ℓ in the buffer zone is proportional to the distance from the wall.
- In the case of free turbulence generated by placing a grid in a uniform stream, ℓ is comparable to the grid size behind the grid, and increases with downstream position.

The inviscid scales are complemented by viscous scales that develop spontaneously inside the fluid.

10.10.6 Viscous scales

Energy is dissipated in a turbulent flow even if the mean flow has a uniform velocity profile. A continuous external supply of energy is necessary to sustain the motion of the fluid. The rate of viscous dissipation, with units of kinetic energy per mass per time, is denoted by

$$\epsilon \, [=] \, \frac{L^2}{T^3}, \tag{10.10.9}$$

where the symbol [=] denotes dimensional equivalence, L is length, and T is time. One distinguishing property of turbulent flow is that dissipation occurs mainly due to small-scale motion.

It can be argued that the rate of dissipation is determined primarily by the fluid properties. Combining ϵ with the kinematic viscosity, ν, we formulate the Kolmogorov length scale

$$\eta \equiv \left(\frac{\nu^3}{\epsilon}\right)^{1/4}, \tag{10.10.10}$$

and accompanying Kolmogorov velocity scale,

$$u_{\mathrm{K}} \equiv (\nu\,\epsilon)^{1/4}. \tag{10.10.11}$$

The two scales are related by

$$\mathrm{Re}_{\mathrm{K}} \equiv \frac{u_{\mathrm{K}}\eta}{\nu} = 1, \tag{10.10.12}$$

where Re_{K} is the Reynolds number of the energy-dissipating motion. By design, Re_{K} is equal to unity, underlying the dominance of viscous forces responsible for converting kinetic to thermal energy inside a viscous fluid.

10.10.7 Relation between inviscid and viscous scales

Energy conservation requires that the rate of viscous dissipation, ϵ, scales as

$$\epsilon \simeq \frac{u^3}{\ell}. \tag{10.10.13}$$

Substituting this estimate into (10.10.10) and rearranging, we obtain

$$\frac{\eta}{\ell} \simeq \left(\frac{\nu}{u\ell}\right)^{3/4}, \tag{10.10.14}$$

where we recall that η is the Kolmogorov length scale.

The magnitude of the velocity fluctuations, u, is typically comparable to the external velocity scale, V, whereas the inviscid length scale ℓ is comparable to the external length scale, L. As a result, the inverse of the ratio on the right-hand side of (10.10.14) is comparable to the Reynolds number $\mathrm{Re} = VL/\nu$, yielding the scaling

$$\frac{\eta}{\ell} \simeq \mathrm{Re}^{-3/4}. \tag{10.10.15}$$

Working in a similar fashion with (10.10.11), we derive the scaling law

$$\frac{u_{\mathrm{K}}}{u} \simeq \mathrm{Re}^{-1/4}, \tag{10.10.16}$$

where we recall that u_{K} is the Kolmogorov velocity scale. These equations allow us to estimate the scales of the energy-dissipating motion from measurable or observable outer scales and the Reynolds number of the flow.

PROBLEMS

10.10.1 *Turbulent mean velocity profile in pipe flow*

Consider turbulent flow in a pipe whose mean velocity profile is described by (10.10.8). Derive a relationship between the mean flow rate and the mean velocity at the centerline. Compare this relationship with its counterpart for laminar Poiseuille flow.

10.10.2 *Kolmogorov length scale for pipe flow*

Laboratory data for turbulent flow in a circular tube with diameter D has shown that: (a) the length scale of the energy containing turbulent motion, ℓ, is comparable to D, and (b) the magnitude of the turbulent velocity fluctuations in comparable to the maximum mean velocity occurring at the centerline, V. Based on this information, compute the Kolmogorov length and velocity scale for a tube with diameter $D = 10$ cm, at Reynolds number $\text{Re} \equiv VD/\nu = 10^6$.

10.11 Spectrum of a turbulent flow

To analyze the distribution of energy across the scales of a turbulent flow, it is helpful to decompose a recording of the velocity or pressure at a particular location into a Fourier series with respect to time, and then examine the magnitude of the Fourier coefficients.

In the laboratory, the velocity is measured typically by two methods: hot-wire anemometry based on a calibration that associates velocity to heat loss from a small heated wire probe placed in a flow; and laser-Doppler velocimetry based on light scattering from a patterned laser beam caused by small particles seeded in the flow.

Time series analysis

To develop the Fourier decomposition, we consider a times series of a function, $f(t)$, consisting of a sequence of values of the function recorded at evenly spaced time intervals separated by a sampling time, Δt. Suppose that the time series contains N records corresponding to times

$$t_1 = 0, \qquad t_2 = \Delta t, \qquad t_3 = 2\,\Delta t, \qquad \ldots, \qquad t_N = (N-1)\Delta t, \tag{10.11.1}$$

and define the total time $T = N\Delta t$. Using Fourier representation theory, and assuming for convenience that $f(N\,\Delta t) = f(0)$, we express the function $f(t)$ over the time interval $(0, T)$ in terms of a complete Fourier series,

$$f(t) \simeq \tfrac{1}{2}\,a_0 + \sum_{p=1}^{M} a_p \cos\Big(\frac{2\pi p}{N}\,\frac{t}{\Delta t}\Big) + \sum_{p=1}^{M} b_p \sin\Big(\frac{2\pi p}{N}\,\frac{t}{\Delta t}\Big) \tag{10.11.2}$$

for $t \geq 0$, where M is a specified truncation level, p is an integer, a_p are cosine Fourier coefficients, and b_p are sine Fourier coefficients.

The complex Fourier coefficients are defined as

$$c_p \equiv \tfrac{1}{2}\,(a_p + \mathrm{i}\,b_p) \tag{10.11.3}$$

for $p = 0, 1, \ldots,$ where i is the imaginary unit, $\mathrm{i}^2 = -1$. In terms of the complex Fourier coefficients, the Fourier series (10.11.2) can be recast into the compact form

$$f(t) \simeq \sum_{p=-M}^{M} c_p \exp\Big(-\,\mathrm{i}\,\frac{2\pi p}{N}\,\frac{t}{\Delta t}\Big), \tag{10.11.4}$$

where the negative-indexed complex Fourier coefficients are given by

$$c_{-p} = c_p^* = \tfrac{1}{2}\,(a_p - \mathrm{i}\, b_p), \tag{10.11.5}$$

and an asterisk denotes the complex conjugate.

Evaluation of the Fourier coefficients

Fourier theory provides us with a remarkably simple method of evaluating the Fourier coefficients.[4] Denoting the data by

$$f_i \equiv f(t_i), \tag{10.11.6}$$

we find that

$$a_p = \frac{2}{N}\,\Big[\, f_1 + \cos(2\pi\,\frac{p}{N})\, f_2 + \cos(2\pi\,\frac{2p}{N})\, f_3 + \cdots + \cos(2\pi\,\frac{(N-1)\,p}{N})\, f_N \,\Big] \tag{10.11.7}$$

and

$$b_p = \frac{2}{N}\,\Big[\, f_1 + \sin(2\pi\,\frac{p}{N})\, f_2 + \sin(2\pi\,\frac{2p}{N})\, f_3 + \cdots + \sin(2\pi\,\frac{(N-1)\,p}{N})\, f_N \,\Big]\,. \tag{10.11.8}$$

In practice, because the number of data points, N, can be on the order of several thousand or even higher, the direct evaluation of the sums on the right-hand sides of expressions (10.11.8) requires a prohibitive amount of computational time. Fortunately, the computations can be expedited considerably by using an ingenious algorithm for computing the Fourier coefficients, known as the fast Fourier transform (FFT).

Function *fft*, located in directory *stats* inside directory *13_turbo* of FDLIB, performs the FFT of a time series with size $N = 2^q$, where q is an integer.

Power spectrum

Now we take the square of both sides of (10.11.4), expand the square of the product on the right-hand side, integrate the resulting expression with respect to time from $t = 0$ to $T \equiv N\,\Delta t$, and use trigonometric identities to set the integral of a large number of terms equal to zero, finding

$$\int_0^T f^2(t)\,\mathrm{d}t \simeq T \sum_{p=-M}^{M} c_p\, c_p^*, \tag{10.11.9}$$

which can be rearranged into

$$\overline{f^2} \equiv \frac{1}{T}\int_0^T f^2(t)\,\mathrm{d}t \simeq \sum_{p=-M}^{M} |c_p|^2 = c_0^2 + 2\sum_{p=1}^{M} |c_p|^2, \tag{10.11.10}$$

---

[4] Pozrikidis, C. (2008) *Numerical Computation in Science and Engineering*, Second Edition, Oxford University Press.

where

$$|c_p|^2 = c_p\, c_p^* = \tfrac{1}{4}\,(a_p^2 + b_p^2) \tag{10.11.11}$$

is the square of the magnitude of the pth complex Fourier coefficient.

A graph of the positive coefficients $2\,|c_p|^2$ against the angular frequency $\omega_p \equiv 2\pi p/\Delta t$ for $p = 1, \ldots,$ is the discrete temporal power spectrum of the function $f(t)$. Of particular interest is the behavior of the power spectrum at high values of p corresponding to high angular frequencies.

A graph of the coefficients $2\,|c_p|^2$ against the spatial wave number $k_p \equiv \omega_p\, V = 2\pi p\, V/\Delta t$ is the discrete power spectrum of the function $f(t)$, where V is a specified velocity. Of particular interest is the behavior at high values of p corresponding to high wave numbers.

Now identifying the generic function $f(t)$ with the x, y, or z component of the velocity, we obtain the discrete energy spectrum of a turbulent flow, providing us with information on the distribution of kinetic energy across different scales.

In practice, the discrete power spectrum is computed by taking the Fourier transform of a time series comprised of sets of data points on the order of $2^{12} = 4096$. The power spectrum computed using one data set exhibits pronounced fluctuations. To obtain a smooth spectrum, the Fourier coefficients are averaged over sets corresponding to different realizations or different time periods for the same flow conditions.

Energy density function

As the sample size, N, and total sampling time, $T = N\Delta t$, tend to infinity, the sum on the right-hand side of (10.11.4) reduces to a Fourier integral. Correspondingly, the right-hand side of (10.11.10) takes the form

$$\overline{f^2} = \int_0^\infty E_t(\omega)\, \mathrm{d}\omega = \int_0^\infty E(k)\, \mathrm{d}k, \tag{10.11.12}$$

where $E_t(\omega)$ and $E(k)$ are temporal and spatial energy density functions. Now making a correspondence between (10.11.12) and (10.11.10), we obtain the relations

$$E_t(\omega_p) = \frac{\Delta t}{2\pi}\, 2\,|c_p|^2, \qquad E(k_p) = \frac{V\Delta t}{2\pi}\, 2\,|c_p|^2, \tag{10.11.13}$$

which allow us to prepare graphs and study the shape of the energy density function. Taylor's frozen-field hypothesis amounts to setting V equal to the local mean value of the streamwise velocity.

FDLIB Data

As an application, we consider a stratified turbulent shear flow behind a vertical grid with mean velocity profile $\overline{u}_x(y)$ and mean temperature field $\overline{T}(y)$, as shown in Figure 10.11.1. At the University of California, San Diego, researcher Kurt Keller recorded a time series of the x

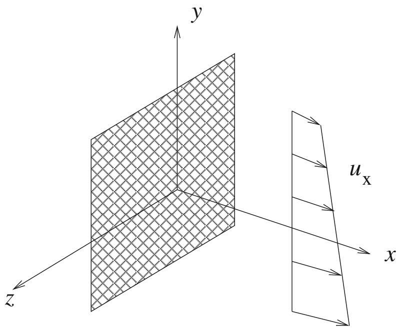

Figure 10.11.1 A time series of the velocity and temperature in stratified turbulent shear flow behind a vertical grid recorded by Kurt Keller can be found in file *keller.dat*, residing in directory *stats* inside directory *13_turbo* of FDLIB.

and y velocity components and temperature at a point located 457.2 cm behind the grid, at the sampling frequency 5 Khz corresponding to sampling time 0.0002 s^{-1}, for the following conditions: grid spacing 2.54 cm; mean shear rate $\mathrm{d}\overline{u}_x/\mathrm{d}y = -7.63\ \mathrm{s}^{-1}$; mean temperature gradient $\mathrm{d}\overline{T}/\mathrm{d}y = 35.8\ \mathrm{K\ m}^{-1}$; local microscale Reynolds number $\mathrm{Re} \equiv \lambda u/\nu = 91.2$.

In the definition of the microscale Reynolds number,

$$u \equiv \sqrt{\overline{u_x'^2}} \tag{10.11.14}$$

is the rms value of the fluctuations of the streamwise component of the velocity and λ is the Taylor microscale defined from the relation

$$\frac{u^2}{\lambda^2} = \overline{\left(\frac{\mathrm{d}u'}{\mathrm{d}y}\right)^2}. \tag{10.11.15}$$

The data are arranged in the three columns of file *keller.dat* located in directory *stats* inside directory *13_turbo* of FDLIB.

PROBLEM

10.11.1 💻 *Stratified shear flow*

(*a*) With reference to Figure 10.11.1, compute and plot the mean and rms values of the velocity and temperature. Investigate their dependence on the sample size.

(*b*) Compute, plot, and discuss the discrete power spectrum of the x and y velocity components and temperature.

10.12 Analysis and modeling of turbulent flow

Deriving exact solutions of the Navier–Stokes equation for turbulent flow is out of the question. Direct numerical simulation (DNS) is prohibited by pragmatic constraints associated with the finite grid size, which necessitate sub-grid modeling: to capture the dynamics of a turbulent flow, we must resolve a prohibitively broad range of length scales. Progress can be made by developing approximate models and phenomenological theories based on empirical correlations that are inspired by laboratory observation.

10.12.1 Reynolds stresses

A useful point of departure for developing phenomenological theories is the decomposition of the velocity field into a mean and a fluctuating component, as shown in equation (10.10.3). A similar decomposition of the pressure field yields

$$p(\mathbf{x},t) = \overline{p}(\mathbf{x},t) + p'(\mathbf{x},t), \tag{10.12.1}$$

where

$$\overline{p}(\mathbf{x},t) \equiv \frac{1}{t_0} \int_{t-\frac{1}{2}t_0}^{t+\frac{1}{2}t_0} p(\mathbf{x}, t+t')\,\mathrm{d}t' \tag{10.12.2}$$

is the mean pressure. The continuity equation for an incompressible fluid requires that

$$\boldsymbol{\nabla}\cdot\overline{\mathbf{u}} = 0, \tag{10.12.3}$$

where a bar denotes the time-averaged value.

Next, we substitute the decompositions (10.10.3) and (10.12.2) into Cauchy's equation of motion, expand the derivatives of the products, take the time average of both sides, and simplify to derive a modified equation of motion for the mean component. The fluctuating component appears as an effective inertial hydrodynamic volume force.

For example, the term $\partial(\rho\, u_x u_y)/\partial y$ on the left-hand side of the x component of the equation of motion (6.3.16), becomes

$$\begin{aligned}\frac{\partial}{\partial y}(\rho\, u_x u_y) &= \frac{\partial}{\partial y}\big[\,\rho\,(\overline{u}_x + u'_x)\,(\overline{u}_y + u'_y)\,\big]\\ &= \frac{\partial}{\partial y}(\rho\,\overline{u}_x\,\overline{u}_y) + \frac{\partial}{\partial y}(\rho\,\overline{u}_x\,u'_y) + \frac{\partial}{\partial y}(\rho\,u'_x\,\overline{u}_y) + \frac{\partial}{\partial y}(\rho\,u'_x\,u'_y).\end{aligned} \tag{10.12.4}$$

Taking the time average of both sides, as shown in equations (10.10.2) and (10.12.2), and interchanging the order of time-averaging and space differentiation, we obtain

$$\begin{aligned}\frac{\partial}{\partial y}(\overline{\rho\,u_x u_y}) &= \frac{\partial}{\partial y}(\overline{\rho\,\overline{u}_x\overline{u}_y}) + \frac{\partial}{\partial y}(\overline{\rho\,\overline{u}_x u'_y}) + \frac{\partial}{\partial y}(\overline{\rho\,u'_x\overline{u}_y}) + \frac{\partial}{\partial y}(\overline{\rho\,u'_x u'_y})\\ &= \frac{\partial}{\partial y}(\rho\,\overline{u}_x\overline{u}_y) + \frac{\partial}{\partial y}(\rho\,\overline{u}_x\overline{u'_y}) + \frac{\partial}{\partial y}(\rho\,\overline{u'_x}\overline{u}_y) + \frac{\partial}{\partial y}(\rho\,\overline{u'_x u'_y}).\end{aligned} \tag{10.12.5}$$

Because of (10.10.4), the second and third terms on the right-hand side of (10.12.5) are zero, leaving the simplified expression

$$\frac{\partial}{\partial y}(\overline{\rho\, u_x u_y}) = \frac{\partial}{\partial y}(\rho\, \overline{u}_x\, \overline{u}_y) + \frac{\partial}{\partial y}(\overline{\rho\, u'_x u'_y}). \tag{10.12.6}$$

RANS

Working in a similar fashion with the other terms on the left-hand side of the Navier–Stokes equation, we derive a the Reynolds-averaged Navier–Stokes (RANS) equation

$$\rho\,(\frac{\partial \overline{\mathbf{u}}}{\partial t} + \overline{\mathbf{u}} \cdot \boldsymbol{\nabla}\overline{\mathbf{u}}) = -\boldsymbol{\nabla}\overline{p} + \mu\, \nabla^2 \overline{\mathbf{u}} + \boldsymbol{\nabla} \cdot \boldsymbol{\sigma}^{\mathrm{R}} + \rho\, \mathbf{g}, \tag{10.12.7}$$

where $\boldsymbol{\sigma}^{\mathrm{R}}$ is the Reynolds stress tensor with components

$$\sigma^{\mathrm{R}}_{ij} = -\overline{\rho\, u'_i u'_j}, \tag{10.12.8}$$

expressing transfer of momentum from the ith to the jth direction, and *vice versa*, by way of turbulence fluctuations. An alternative form of (10.12.7) is

$$\frac{\partial\,(\rho\, \overline{\mathbf{u}})}{\partial t} + \boldsymbol{\nabla} \cdot (\rho\, \overline{\mathbf{u}}\, \overline{\mathbf{u}}) = -\boldsymbol{\nabla}\overline{p} + \mu\, \nabla^2 \overline{\mathbf{u}} + \boldsymbol{\nabla} \cdot \boldsymbol{\sigma}^{\mathrm{R}} + \rho\, \mathbf{g}. \tag{10.12.9}$$

Phenomenological theories seek to establish a relationship between the Reynolds stresses and the structure of the time-averaged flow. Once this has been done, the averaged equation of motion (10.12.7) or (10.12.9) can be solved together with the time-averaged continuity equation (10.12.3) to generate the velocity distribution in a turbulent flow.

The Boussinèsq's law

Boussinèsq proposed the constitutive law

$$\boldsymbol{\sigma}^{\mathrm{R}} = -\tfrac{3}{2}\, \rho k\, \mathbf{I} + \mu_{\mathrm{T}}\, 2\, \overline{\mathbf{E}}, \tag{10.12.10}$$

where

$$k = \tfrac{1}{2}\,(u'^2_x + u'^2_y + u'^2_z) \tag{10.12.11}$$

is the turbulent kinetic energy, μ_{T} is an eddy viscosity, $\mathbf{I}$ is the identity matrix, and $\overline{\mathbf{E}}$ is the time-averaged rate-of-deformation tensor. The scalar $\frac{3}{2}\rho\, k$ in the first term on the right-hand side of (10.12.10) plays the role of a positive turbulence pressure.

In the k-ϵ model, the turbulent kinetic energy is related to the rate of viscous dissipation, ϵ, by

$$\nu_{\mathrm{T}}\, \epsilon = c_\mu\, \rho\, k^2, \tag{10.12.12}$$

where

$$\epsilon = \nu_{\mathrm{T}}\, \overline{\Big(\frac{\partial u_i}{\partial x_j}\Big)\Big(\frac{\partial u_i}{\partial x_j}\Big)}, \tag{10.12.13}$$

$\nu_{\mathrm{T}} = \mu_{\mathrm{T}}/\rho$ is the turbulent kinematic viscosity, c_μ is a dimensionless coefficient, and summation is implied over the repeated indices i and j.

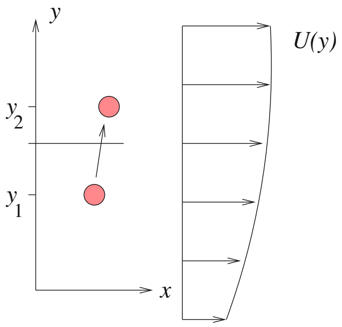

Figure 10.12.1 Profile of turbulent shear flow along the x axis illustrating the random displacement of a fluid parcel by a distance that is comparable to the Prandtl mixing length.

10.12.2 Prandtl's mixing length

Prandtl proposed a physically intuitive model that relates the Reynolds stresses to the velocity profile of the mean flow. Motivation is provided by a tentative analogy between eddy motion in a turbulent flow and molecular motion in a gas. The derivation is similar to that discussed in Section 4.4.5 concerning the fluid viscosity.

Consider a unidirectional turbulent shear flow along the x axis with mean velocity profile $\bar{u}_x = U(y)$, as illustrated in Figure 10.12.1. Suppose that, because of the turbulent motion, a small fluid parcel with volume δV_p, initially located at $y = y_1$, is displaced to the position $y = y_2$ where it travels in the streamwise direction with the new local velocity. The change in the x component of the parcel momentum is

$$\big(\delta M_x\big)_p = \big(\, u_{x(y=y_2,t)} - u_{x(y=y_1,t)} \,\big)\, \rho\, \delta V_p. \tag{10.12.14}$$

Because turbulent fluctuations have been assumed small, the total velocity has been approximated with the mean velocity to give

$$\big(\delta M_x\big)_p \simeq \big(\, U_{(y=y_2)} - U_{(y=y_1)} \,\big)\, \rho\, \delta V_p. \tag{10.12.15}$$

Next, we consider the transport of momentum across a horizontal plane located at elevation y, as shown in Figure 10.12.1. During a small period of time, Δt, all parcels residing inside a layer of thickness $u_y(y,t)\,\Delta t$ adjacent to this elevation cross the elevation to find themselves on the other side. The total volume of fluid crossing the plane is

$$\delta V = u_y(y,t)\, w\, \Delta x\, \Delta t, \tag{10.12.16}$$

where w is an arbitrary width along the z axis. The associated transport of x momentum across a horizontal length Δx due to this motion is

$$\delta M_x \simeq \rho \big[\, U(y=y_2) - U(y=y_1) \,\big]\, \delta V, \tag{10.12.17}$$

which can be approximated as

$$\delta M_x \simeq (y_2 - y_1)\, \frac{\partial U}{\partial y}\, \rho\, \delta V. \tag{10.12.18}$$

Substituting (10.12.16), we obtain

$$\delta M_x \simeq \rho\, u_y(y,t)\, (y_2 - y_1)\, \frac{\partial U}{\partial y}\, w\ \Delta x\, \Delta t. \tag{10.12.19}$$

Averaging this expression over all time intervals, Δt, we obtain

$$\overline{\delta M_x} \simeq \rho\, \overline{u_y(y,t)\, (y_2 - y_1)}\, \frac{\partial U}{\partial y}\, w\, \Delta x\, \Delta t. \tag{10.12.20}$$

According to Newton's second law of motion, this averaged transfer of momentum amounts to a force pointing in the x direction, expressed by the Reynolds shear stress, σ^{R}_{xy}. Setting

$$\overline{\delta M_x} = \sigma^{\mathrm{R}}_{xy}\, w\, \Delta x\, \Delta t \tag{10.12.21}$$

and rearranging, we obtain

$$\sigma^{\mathrm{R}}_{xy} = \rho\, \overline{u_y(y,t)\, \Delta y}\, \frac{\partial U}{\partial y}. \tag{10.12.22}$$

where $\Delta y \equiv y_2 - y_1$.

In the next key step, we introduce the scaling

$$\overline{u_y(y,t)\, \Delta y} \simeq \sqrt{\overline{u'^2_y}}\, \ell_{\mathrm{P}} \simeq \left| \frac{\partial U}{\partial y} \right| \ell_P^2, \tag{10.12.23}$$

where ℓ_{P} is Prandtl's mixing length. Substituting (10.12.23) into (10.12.22), we obtain the targeted constitutive equation

$$\sigma^{\mathrm{R}}_{xy}(y) = \rho\, \ell_{\mathrm{P}}^2 \left| \frac{\partial U}{\partial y} \right| \left(\frac{\partial U}{\partial y} \right). \tag{10.12.24}$$

The product of the first three terms on the right-hand side of (10.12.24) plays the role of the eddy viscosity introduced by Boussinèsq.

Readers who are overwhelmed by uneasiness regarding the physical relevance of the various steps involved in the preceding derivation are not alone. Numerous constitutive relations similar to that shown in (10.12.24) have been proposed based on heuristic and tentative analogies and laboratory observation.

10.12.3 Logarithmic law for wall-bounded shear flow

As an application, we use Prandtl's mixing length model expressed by equation (10.12.24) to deduce the functional form of the velocity profile in wall-bounded shear flow, away from the viscous sublayer and the buffer zone.

Assuming that the sign of $\mathrm{d}U/\mathrm{d}y$ is positive, neglecting the viscous shear stress $\mu\,\mathrm{d}U/\mathrm{d}y$ in comparison to the Reynolds shear stress, and ignoring the variation of the shear stress in the y direction due to the streamwise pressure drop, we find that

$$\sigma^{\mathrm{R}}_{xy}(y) = \rho\,\ell_{\mathrm{P}}^2 \left(\frac{\mathrm{d}U}{\mathrm{d}y}\right)^2 = \tau_{\mathrm{wall}}, \tag{10.12.25}$$

where τ_{wall} is the wall shear stress. Rearranging, we obtain

$$\ell_{\mathrm{P}}^2 \left(\frac{\mathrm{d}U}{\mathrm{d}y}\right)^2 = \frac{\tau_{\mathrm{wall}}}{\rho} \equiv u_*^2, \tag{10.12.26}$$

where u_* is the friction velocity.

Next, we set the Prandtl mixing length proportional to the distance from the wall,

$$\ell_{\mathrm{P}} = \kappa\,y, \tag{10.12.27}$$

where κ is a dimensionless constant. In the case of flow through a circular tube, measurements suggest the particular value $\kappa \simeq 0.36$. Substituting (10.12.27) into (10.12.26), taking the square root of the emerging equation, and rearranging, we find that

$$\frac{\mathrm{d}U}{\mathrm{d}y} = \frac{u_*}{\kappa y}. \tag{10.12.28}$$

Integrating with respect to y, we derive the logarithmic relationship

$$\frac{U(y)}{u_*} = \frac{1}{\kappa}\ln\frac{y}{a} + A, \tag{10.12.29}$$

where a is a defined length and A is a dimensionless constant. In dimensionless variables, expression (10.12.29) takes the form

$$u^+ = \frac{1}{\kappa}\ln y^+ + B, \tag{10.12.30}$$

where B is another dimensionless constant, and we have defined

$$u^+ \equiv \frac{\overline{u}_x(y)}{u_*} = \frac{U(y)}{u_*}, \qquad y^+ \equiv \frac{u_* y}{\nu}. \tag{10.12.31}$$

Laboratory measurements have shown that equation (10.12.30) with $B = 3.6$ describes accurately the velocity profile approximately for $y^+ > 26$, as illustrated in Figure 10.12.2.

In the viscous sublayer attached to the wall, laboratory observations suggest the linear relation

$$u^+ = y^+ \tag{10.12.32}$$

approximately for $0 < y^+ < 5$. In the buffer zone, $5 < y^+ < 26$, a more involved relation is required.

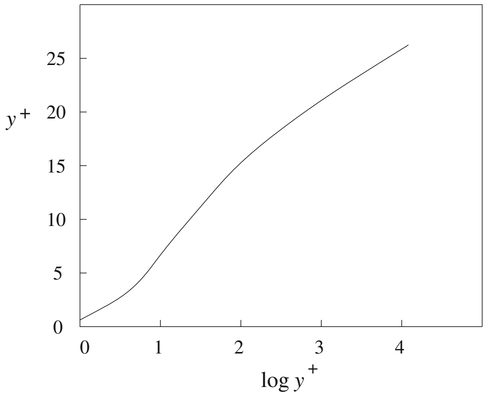

Figure 10.12.2 Schematic illustration of the distribution of the mean velocity in the dimensionless variables defined in equations (10.12.31) for wall-bounded turbulent shear flow.

10.12.4 Correlations

Space-time correlations allow us to extract information on the small-scale structure of a turbulent flow. Consider the ith component of the fluctuating velocity at a point, $\mathbf{x}_1$, at time t, and the jth component of the fluctuating velocity at another point, $\mathbf{x}_2$, at time $t+\tau$, where τ is the time delay. The corresponding second-order space-time correlation is defined as

$$\mathcal{R}_{ij}(\mathbf{x}_1, \mathbf{x}_2, t, \tau) \equiv \overline{u_i'(\mathbf{x}_1, t)\, u_j'(\mathbf{x}_2, t+\tau)}. \tag{10.12.33}$$

Explicitly,

$$\mathcal{R}_{ij}(\mathbf{x}_1, \mathbf{x}_2, t, \tau) = \frac{1}{t_0} \int_{t-\frac{1}{2}t_0/2}^{t+\frac{1}{2}t_0} u_i'(\mathbf{x}_1, t+t')\, u_j'(\mathbf{x}_2, t+\tau+t')\, \mathrm{d}t'. \tag{10.12.34}$$

Two special correlations are of particular interest: the spatial correlation corresponding to $\tau = 0$, and the time-delayed correlation arising when the points $\mathbf{x}_1$ and $\mathbf{x}_2$ coincide.

Taylor's frozen-field hypothesis provides us with a relationship between the time-delayed and spatial correlation. The underlying reasoning is that, in a low-intensity turbulent flow, the mean velocity sweeps the turbulence so fast that the eddies do not evolve significantly during the time it takes them to cross a fixed point in space. Physically, the velocity vector field appears to be frozen in time. If the mean velocity is in the direction of the x axis, we may write

$$\mathcal{R}_{ij}(\mathbf{x}_1, \mathbf{x}_2, t, \tau) \simeq \mathcal{R}_{ij}(\mathbf{x}_1, \mathbf{x}_1 + \Delta x\, \mathbf{e}_x, t, \tau) = \mathcal{R}_{ij}\big(\mathbf{x}_1, \mathbf{x}_1, t, \tau = -\frac{\Delta x}{\overline{u}_x}\big), \tag{10.12.35}$$

where $\mathbf{e}_x$ is the unit vector along the x axis. This expression provides us with a convenient method for obtaining a spatial correlation in terms of a more accessible time-delayed correlation.

The usefulness of second-order correlations lies in their ability to provide us with information on the geometrical structure and dynamics of eddy motion in a turbulent flow. As a point $\mathbf{x}_2$ tends to another point $\mathbf{x}_1$, local fluid motions are coordinated and the correlations are significant. As the points $\mathbf{x}_1$ and $\mathbf{x}_2$ move farther apart, the fluid motions become independent or uncorrelated and the correlations decay to zero.

Homogeneous and isotropic turbulence

In the case of homogeneous turbulent flow, the correlations depend on the vectorial distance between the points $\mathbf{x}_1$ and $\mathbf{x}_2$, but not on the absolute position of each point. To signify this dependence, we write

$$\mathcal{R}_{ij}(\mathbf{x}_2 - \mathbf{x}_1, t, \tau). \tag{10.12.36}$$

In the case of isotropic turbulent flow, the correlations depend on the scalar distance between the two points, $|\mathbf{x}_2 - \mathbf{x}_1|$. To signify this dependence, we write

$$R_{ij}(|\mathbf{x}_2 - \mathbf{x}_1|, t, \tau). \tag{10.12.37}$$

Evolution equations

Evolution equations for second-order correlations can be derived from the Navier–Stokes equation. Just as the averaged Navier–Stokes equation (10.12.7) involves the Reynolds stresses, evolution equations for second-order correlations involve third-order correlations defined as time averages of products of three scalar fluctuating components. An important field of study in the general subject of turbulent flow seeks to establish relations between high-order correlations and the structure of the mean flow, thereby achieving closure.

Problems

10.12.1 *Deissler correlation*

Deissler replaced Prandtl's constitutive equation (10.12.24) with a more involved equation inspired by laboratory measurements,

$$\sigma_{xy}^{R}(y) = n^2 \rho\, y\, U(y) \left(\frac{\partial U}{\partial y}\right)_y \big(1 - \exp(-\frac{n^2 U y}{\nu})\big), \tag{10.12.38}$$

where $n = 0.124$ is an experimentally determined dimensionless constant. Substitute this relation into (10.12.25), integrate to compute the velocity profile, and then compare the profile with that shown in (10.12.30).

10.12.2 💻 *Stratified shear flow*

Compute, plot, and discuss the form of the time-delayed correlation of the velocity components and temperature recorded in file *keller.dat* residing in directory *stats* inside directory *13_turbo* of FDLIB.